Multi-scale modelling of Lithium-ion batteries: From transport phenomena to the outbreak of thermal runaway

Tomaž Katrašnik [*], Igor Mele, Klemen Zelič

University of Ljubljana, Faculty of Mechanical Engineering, Laboratory for Internal Combustion Engines and Electromobility, Aškerčeva 6, Ljubljana SI-1000, Slovenia

ARTICLE INFO

ABSTRACT

Multi-scale and multi-domain mathematical models capable of modelling main electrochemical reactions, side reactions and heat generation can reduce the time and cost of lithium-ion battery development and deployment, since these processes decisively influence performance, durability and safety of batteries. Experimental evidences clearly indicate the importance of the interplay between electric and thermal boundary conditions, cell design and applied materials, side reactions as well as safety implications of batteries, which are not yet captured to a sufficient level by simulations models. As an answer to this challenge, the paper presents an advanced multi-scale battery modelling framework that can be seamlessly integrated into multi-domain models. The key hypothesis is that nanoscopic transport phenomena and resulting heat generation decisively influence the entire chain of mechanisms that can lead to the outbreak of the thermal runaway. This is confirmed by developing a multi-scale battery modelling framework that is based on the continuous modelling approach featuring more consistent virtual representation of the electrode topology and incorporating the coupled chain of models for heat generations and side reactions. As a result, the battery modelling framework intuitively yet insightfully elucidates the entire chain of phenomena from electric and thermal boundary conditions, over cell design and properties of applied materials to solid electrolyte interphase growth, its decomposition and subsequent side reactions at the anode, cathode and the electrolyte that lead to the thermal runaway. One of key results comprises multi-level main and side reaction driven heat transfer cross-talk between the anode and the cathode. Therefore, the presented advanced multi-scale battery modelling framework represents a contribution to the advanced virtual development of batteries thereby contributing to tailoring battery design to a specific application.

1. Introduction

Batteries are one of the key enablers for complying with the Paris Declaration on Climate Change. Batteries are also one of the most widespread energy storage devices and a key component in future energy systems and devices. They are thus enablers for more sustainable mobility and more user-friendly leisure applications, and with the introduction of renewable energy sources, they are gaining significance in energy applications.

This broad range of applications shares certain common high-level objectives, which can be summarised as: higher energy and power density, prolonged life and increased safety of batteries, which will be produced using abundant materials, and which will comply with the principles of circular economy while simultaneously featuring low costs [1]. Additionally, this broad range of applications imposes several application-specific objectives, which cover operating temperatures,

specific load profiles, and specific durability and safety criteria. Therefore, a single design cannot optimally fulfil all these requirements. Thus, tailoring battery design to a specific application with the aim of approaching engineering limits presents a significant challenge.

Hence, several types of active electrode materials, electrolytes, electron conducting materials, coatings and binders are used in the production of Li-ion batteries, e.g. [2]. Such a variety of materials also inherently reflects their different dynamics of main reactions, i.e. Li (de) intercalation dynamics [2], and even more pronounced differences in degradation and safety relevant side reactions. Regarding (de) intercalation dynamics, the materials and lattice structures dictate different equilibrium chemical potentials and diffusion paths in the host matrix, e. g. [3], while the size distribution of individual primary particles and secondary particles, that is, agglomerates, also influences overpotentials at different rates of (de) lithiation.

In addition, it is well known that battery performance, and safety in particular, crucially depend on the degradation phenomena, which

Nomenclature

Abbreviations

AET	Advanced Electrode Topology
B + CF	Binder and Conductive Filler
DoD	Depth of Discharge
LFP	Lithium Iron Phosphate
LCO	Lithium Cobalt Oxide
LMO	Lithium Manganese Oxide
LPL	Lithium plating
NCA	Lithium Nickel Cobalt Aluminium oxide
NCM	Lithium Nickel Cobalt Manganese oxide
RT	Real Time
SEI	Solid Electrolyte Interphase
STXM	Scanning Transmission X-ray Microscopy
TEM	Transmission Electron Microscope

Greek letters

α	Charge transfer coefficient [–]
α_{pe}	Degree of conversion of the positive electrode active material [–]
δ	Thickness [m]
ϵ	Porosity [–]
η	Overpotential [V]
κ	Liquid phase conductivity [S/m]
λ	Thermal conductivity [W/m K]
μ	Chemical potential [J/mol]
Ω	Regular solution parameter [J/mol]
ω	Fraction [–]
Φ	Potential [V]
ϕ	Ratio [–]
ρ	Density [kg/m^3]
σ	Solid phase conductivity [S/m]

Latin letters

$\bar{c}$	Average concentration [mol/m^3]
$\hat{n}$	unity vector normal to the surface [–]
$\mathscr{F}$	Total free energy [J/mol]
$\mathscr{K}$	Gradient penalty coefficient [eV/m]
D	Diffusion constant [m^2/s]
A	Surface [m^2]
a	Specific surface [m^2/m^3]
A_f	Frequency factor [1/s]
B	Phase boundary strain [GPa]
c	Concentration [mol/m^3]
c_p	Specific heat [J/kg K]
$\vec{N}$	Diffusion flux in solid [mol/m^{2}s]
E_a	Activation energy [J/mol]
F	Faraday constant [As/mol]
$f_\pm$	Activity coefficient [–]
H	Enthalpy of reaction [J/kg]
h	Specific enthalpy [J/mol]
I	Current density [A/m^2]
i	Molar flux [mol/m^{2}s]
j	Molar flux [mol/m^{2}s]
k_0	Kinetic rate constant [m/s]
k_B	Boltzmann constant [J/K]
L	Size [m]
M	Molar mass [kg/mol]
P	Permeability of the connection [m/s]
q	Heat generation per unit of volume [W/m^3]
R	Gas constant [J/mol K]
r	Radial coordinate [m]
s	Specific entropy [J/mol K]
T	Temperature [K]
t_+	Transference number [–]
U	Standard potential [V]
X	Molarity [mol/m^3]
x	Filling fraction [–]

Subscripts or superscripts

e	Electrolyte
k	Particle index
l	Particle-to-particle connection index
s	Solid
app	Applied
b + cf	Binder and conductive filler
brugg	Bruggeman factor
D	Decomposition
DC	Direct-contact
EC	Ethylene carbonate
eff	Effective
EQ	Equilibrium
FILM	Passivated film
Li	Lithium
Li,ts	Lithium transport in solid
Li-el	Lithium-electrolyte
LPL	Lithium plating
max	Maximal
ohm	Ohmic
react	Reaction
ref	Reference
rev	Reversible
SEI	Solid Electrolyte Interphase
SEI$_D$	Solid Electrolyte Interphase Decomposition
SURF	Surface
tot	Total
V	Volume

occur at different time and length scales thus calling for advanced in situ and ex situ analysis techniques [4]. Batteries are subjected to several degradation phenomena [5], whereas the reactions of solid electrolyte interphase (SEI) formation, decomposition, and subsequent reactions between anode and electrolyte, i.e. SEI regeneration, are one of the prominent causes of the outbreak of the thermal runaway at slightly elevated temperatures, e.g. [6]. These exothermic reactions might increase the temperature to a level promoting cathode-electrolyte reactions, e.g. [7], oxygen dissolution from active, in particular cathode, materials, e.g. [8], and electrolyte decomposition reactions [9]. Furthermore, dissolution of metal ions from the cathode, which is also promoted at elevated temperatures, and their transport to the anode further promotes growth of SEI, e.g. [10]. This chain of phenomena,

which is associated with multiple exothermic reactions, is an important safety critical aspect of battery incorporating liquid electrolytes, e.g. [11].

Although there is a consensus on the strong impact of the SEI related phenomena on battery performance and safety, a nanoscopic understanding of how the SEI evolves with battery ageing remains limited due to the difficulty in characterising the structural and chemical properties of this sensitive interphase [12]. Different experiments have revealed that the SEI exhibits a dual-layer structure with a dense inner layer and a porous outer layer [13]. Furthermore, ref [12] also reports on the diversity of observed SEI morphologies suggesting that SEI growth is a highly heterogeneous process. This heterogeneity further aggravates by the facts that SEI growth rate and composition is influenced by (among

others): electrolyte composition [14]; the electrolyte salt [15]; deposition of metals on the graphite electrode, e.g. [16]; smoothness of the SEI surface [17].

Limited understanding of how the SEI evolves with battery ageing further aggravates when addressing SEI decomposition and regeneration phenomena, e.g. [18]. The literature already offers several inspiring experimental calorimetric studies on the temperature ranges of the selected mechanisms and the resulting released heats that lead to the subsequent onset of thermal runaway [19]. However, detailed mechanisms of the SEI decomposition and regeneration phenomena as well as subsequent reactions in the thermal runaway chain that comprise previously mentioned cathode-electrolyte reactions and electrolyte decomposition reactions as well as chemistry specific additional side reactions are even less researched and elaborated as SEI formation mechanisms owing to the complexity of the underlying mechanisms.

One of the crucial approaches for tailoring battery design to a specific application and to cope with the addressed complexity of underlying phenomena relies on virtual prototyping in the early development phases being one of the key enablers of the front-loading of the development process [1]. A huge variation space covering material selection and geometrical characteristics from the nano- to the macro-scale as well as the resulting reaction and transport phenomena occurring at very large spans of length- and time-scales inherently requires multi-scale modelling and simulation support to create high fidelity virtual prototypes, which are one of the enablers for achieving the listed objectives [20]. It is well known that a single computational model encompassing all relevant phenomena and scales is beyond the limits of current computing power and methods [21]. Current battery models are thus not yet capable of providing full answers to the multi-scale challenges [21] and, in particular, to address the interplay between electric and thermal boundary conditions, cell design and applied materials, side reactions and safety implications of batteries. Therefore, it is of utmost importance to further develop the building blocks of multi-scale modelling approaches, which is the main motivation of this paper.

Currently, models on particular scales are, in general, tailored to simulate dedicated phenomena [21]. Hence, continuum scale has proven as an appropriate scale for supporting analyses on the level of a single electrochemical cell during long term transient simulations. In general, continuum porous electrode battery models are based on or inspired by the pioneering work in the field of porous electrode theory published by Newman et al. in 1975 [22]. As analysed in [3], Newman theory features certain deficiencies in the context of the present requirements of advanced battery models. Namely, continuum models generally rely on an oversimplified topological representation of electrodes, where particles in a model represent homogeneous and frequently spherical secondary particles. As analysed in [3] this can introduce significant deviations in transport properties for certain materials and topologies of secondary particles as for example for the lithium iron phosphate Li_xFePO_4 (LFP). In addition, the concentrations and potentials of active cathode and anode particles are usually calculated by Fick's second law of diffusion, e.g. [23] and fitted voltage vs. depth of discharge (DoD) curves. This might introduce fundamental physiochemical inaccuracies to the model that are usually further corrected by the adjustment of fitting parameters rather than by incorporating upscaled fundamentals from atomistic- and mesoscale phenomena in the models. This leads to a compromised prediction capability of electric output of such models [3], whereas it even more profoundly influences intra-cell and intra-electrode transport phenomena.

Electrochemical models, based on the Newman approach, are often upgraded with the thermal model, e.g. [24], where the energy equation is solved with the corresponding reversible and irreversible heat losses that originate from the local concentration and potential fields. References, such as [25,24] and many other, model combination of LFP cathode and graphite anode. These references do not consider inter primary particle exchange of Li, being inherent to this type of phase

separating material at low currents and thus local overpotentials [26], thus disregarding heat generation sources associated with this transport phenomenon. Resultantly, these deficiencies are even more pronounced when modelling degradation phenomena, which are driven by local concentration, potential, and temperature fields.

Several modelling approaches have already been developed to address the topic of side reactions or degradation phenomena. These range from first principle computations, e.g. [27] of specific degradation phenomena to phenomenological and empirical models of SEI and Li plating, e.g. [10], yielding model outputs on the continuum level, i.e. on a particle level or on the control volume/electrode level. Reference [18] proposes an insightful approaches for coupling a basic electrochemical model and degradation models relevant to the onset of thermal runaway. The proposed approach [18] is based on coupling plausible set of relevant degradation equations to the zero dimensional electrochemical battery model. Although such an approach offers several interesting results [18], Ref. [28] demonstrates importance of considering spatially resolved degradation phenomena coupled to the electrochemical model when virtually assessing degradation phenomena during battery operation. Inspiring model of [28] was designed to study the interplay between SEI formation and Li plating and it, therefore, expectedly lacks of several equations of degradation mechanisms relevant for the onset of thermal runaway. It can thus be concluded that the modelling framework encompassing the interplay between electric and thermal boundary conditions, cell design and applied materials, and thus spatially plausible representation of electrodes, side reactions and safety implications of batteries that is applicable for modelling these coupled phenomena during battery cycling is still missing.

To provide an answer to these challenges and to further develop the building blocks of multi-scale modelling approaches, this paper proposes an advanced multi-scale battery modelling framework that establishes a consistent causal chain from material properties, crystallographic structure of the cathode material, over electrode topology, main and side reactions and heat generation to the outbreak of thermal runaway. This is achieved by originating from the recently published advanced porous electrode modelling framework based on more consistent virtual representation of the electrode topology [3] and developing an advanced multi-scale battery modelling framework capable of incorporating the coupled chain of models for main transport and electrochemical phenomena, side reactions and heat generation. The modelling framework thus innovatively introduces cross-influencing terms between governing equations for modelling main and side reactions as well as heat generation. It furthermore proposes an innovative heat generation term due to inter primary particle transport of Li, which is made possible by more consistent, mesoscale inspired, representation of the electrode topology virtually represented by agglomerates of primary particles. These transport, electrochemical and thermal models are further coupled to models of SEI formation [28], SEI decomposition [18], SEI regeneration [18], cathode decomposition [9] and electrolyte decomposition [9], which were formulated in a way to comply with the particle based formulation of electrode models. The developed multi-scale battery modelling framework covering multiple intertwined processes is thus innovatively applied to model outbreak of the thermal runaway during battery cycling using a heterogeneous, spatially and temporally resolved model.

To create a challenging virtual test case and to expose the complex interaction of intra-cell phenomena LFP material, characterised by being phase-separating and featuring fast diffusion in one dimension as well as complex mesoscale topology of the secondary particles, is selected as a cathode material. It is paired with the graphite anode. This pair of materials has wide application area, while due to low price of LFP-graphite batteries they are one of the suitable candidates also for widespread stationary applications and for specific mobile applications.

Proposed modelling framework based on the multi-scale approach applied to LFP-graphite cell was used to demonstrate the need to preserve consistency to lower scales when modelling coupled phenomena.
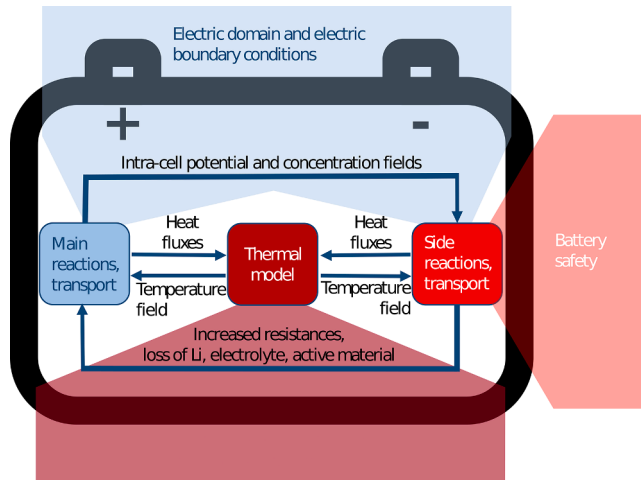
Fig. 1. Schematic representation of the interactions between main and side reactions including transport phenomena and the heat generation with corresponding domain specific boundary conditions and indicated safety implications.

In addition, it was used to confirm hypothesis that nanoscopic transport phenomena and resulting heat generation decisively influence the entire chain of mechanisms that can lead to the outbreak of the thermal runaway. This is beside more consistent, mesoscale inspired, topological representation of electrode reflected also through an advanced and consistent scale bridging methods to calculate chemical potentials of the primary LFP particles [29] based on multi-scale sequential linking approach [30].

As a result, the proposed battery modelling framework intuitively yet insightfully elucidates the entire chain of phenomena from electric and thermal boundary conditions, over cell design and properties of applied materials to solid electrolyte interphase growth, its decomposition and subsequent side reactions at the anode, cathode and the electrolyte that lead to the outbreak of the thermal runaway. One of key results comprises multi-level main and side reaction driven heat transfer cross-talk between the anode and the cathode. The proposed approach, therefore, enables the preservation of consistency to lower scales, and delivers spatially and temporally resolved results while achieving computational times that enable efficiently support of long-term degradation analyses.

2. Modelling framework

This section presents the governing equations of the advanced multi-scale modelling framework, which establish a consistent link from crystallographic structure of the cathode, over electrode topology, heat generation, and degradation phenomena, to the outbreak of the thermal runaway. Section 2.1 describes the electrochemical and transport equations, inspired by mesoscale transport phenomena and incorporating scale bridging methods to calculate chemical potentials of the primary LFP particles, formulated on the continuum scale. Section 2.2 focuses on the degradation mechanisms at the anode, specifically the SEI

formation (Section 2.2.1) and SEI decomposition processes (Section 2.2.2), the reaction of intercalated Li with the electrolyte (Section 2.2.3), the deposition of metallic Li (Section 2.2.4), and the calculation of film thickness on the anode particles (Section 2.2.5); degradation of cathode active material (Section 2.2.7); and electrolyte decomposition (Section 2.2.6). Finally, Section 2.3 describes the thermal model that matches the level of depth of the electrochemical and the transport model.

Although demonstrated on LFP-graphite cells, the proposed modelling framework can be applied to other materials by adjusting the inherent material parameters and material-specific topological parameters and incorporating other models of main and side reactions.
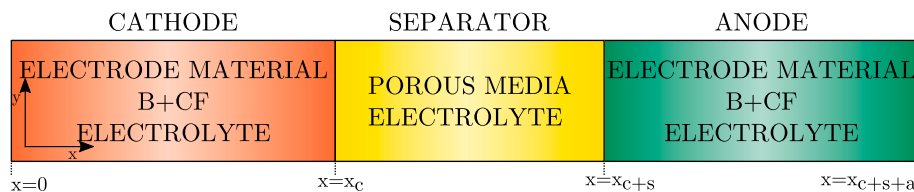
A basic schematic representation of the multi-scale battery modelling framework that comprises interactions between main and side reactions including transport phenomena and the heat generation with corresponding domain specific boundary conditions and indicated safety implications is given in Fig. 1. Functionality of this modelling framework is in this paper demonstrated on one dimensional (1D) computational domain featuring a full cell with cathode, separator and anode, and the corresponding boundary conditions as presented in Fig. 2. In addition, Fig. 3 presents a more detailed schematics of the modelling concept presented in Fig. 1 applied to the computational mesh presented in Fig. 2. Fig. 3 graphically depicts more consistent, mesoscale inspired, topological representation of electrode topology applied in the continuum model and functionalities and positions models of side reactions. From this representation, cross-interaction between main and side reactions is discernible, while they all contribute to heat fluxes.

2.1. Electrochemical and transport model

To preserve the brevity and completeness of the model descriptions, previously published equations will be briefly summarised in Appendices: A.2 and A.3, whereas emphasis will be devoted to the innovatively extended equations. A mesoscale inspired topological representation of electrode topology is based on the recently published advanced porous electrode modelling framework based on more consistent virtual representation of the electrode topology [3], which is extended to adequately interact with heat generation and side reaction phenomena. In the presented work, this more consistent topological representation of the electrode topology will be demonstrated on the LFP material characterised by being phase-separating and featuring very complex non-spherical agglomerates (Fig. A.1).

Fig. 3 presents, on the cathode side, advanced particle connectivity approach enabling modelling materials with significantly different topologies of active material by virtually creating agglomerates, representing secondary particles, from primary particles. This establishes the link between the mesoscopic scale with a detailed three dimensional (3D) representation of electrode topology and the approach to model these phenomena on the continuum single cell scale. As reported in [3], proposed generic modelling framework also allows for seamless replication of modelling functionality of previously published porous electrode modelling approaches including Newman based modelling approach, as presented in Section 3.1.

To preserve consistency to lower scales, multi particle size distribution is implemented in such a way that each computational cell can host

Fig. 2. Schematic of the computational domain featuring full cell with cathode, separator and anode. Both electrodes consist of an active electrode material, a combined volume fraction of binder and conductive filler (carbon black) denoted by the label B + CF and a liquid electrolyte, whereas the separator is represented with a non-conductive porous media soaked with the liquid electrolyte.
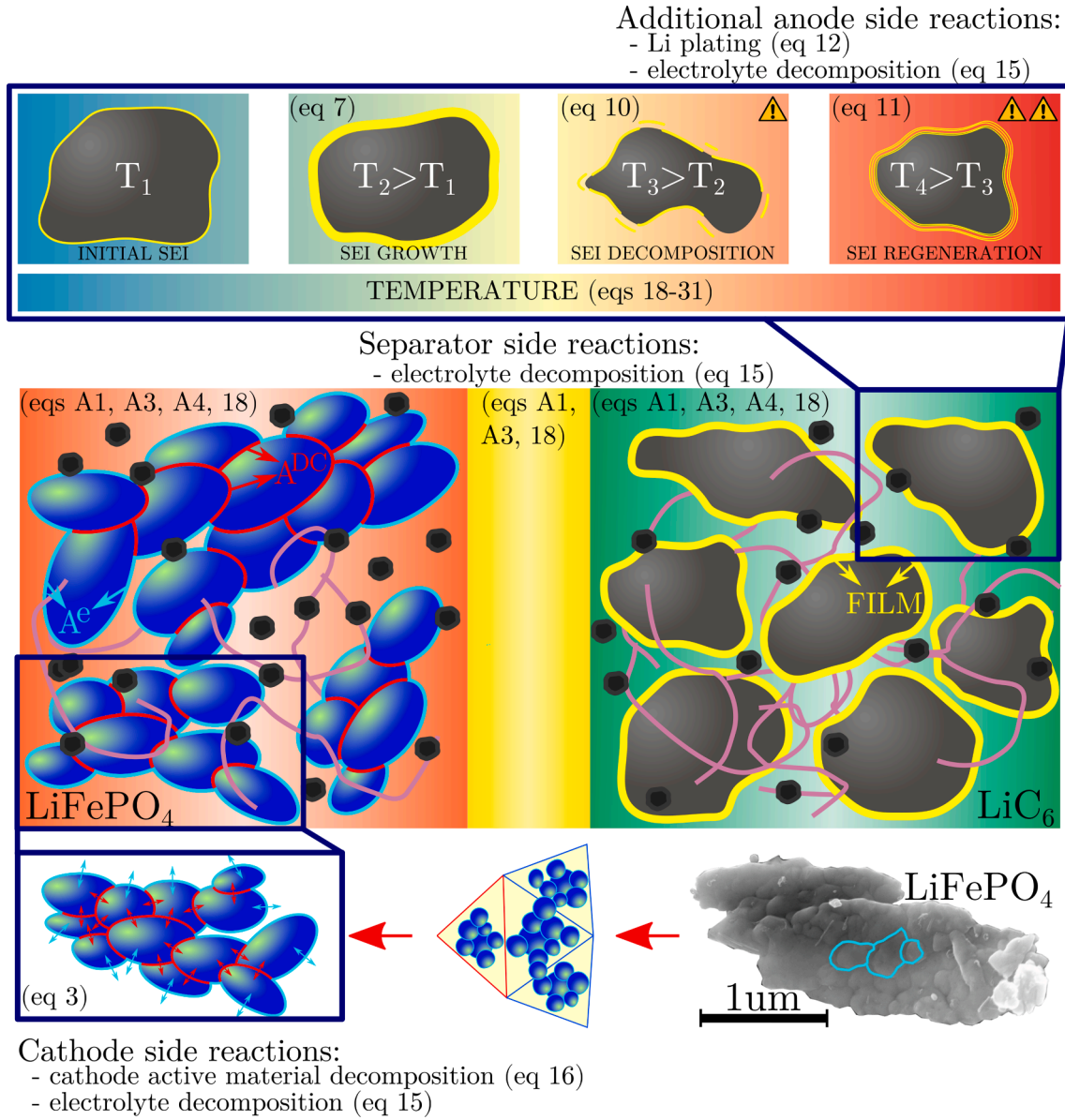
Fig. 3. A more detailed schematic representation of the interactions between main and side reactions including transport phenomena and the heat generation with indicated mesoscale inspired topological representation of electrode topology and depicted and listed modelled side reactions. Figure also includes references to the main governing equations for modelling specific phenomena.

an arbitrary number of representative particles with arbitrary size distribution and interconnected as presented in Fig. 3. This approach enables consistent topological representation of real topological structure of the electrodes, as presented here for the LFP material (Fig. A.1).

Primary particles are thus interconnected into agglomerates by the connectivity scheme that allows for the decoupling of a single particle's total surface between the surface in contact with the electrolyte (A^e) and the surface of direct connections to neighbouring particles (A^{DC}), which can be written as

$$A_k = A_k^e + \sum_l A_{k,l}^{DC},\qquad(1)$$

where indexes k and l denote the index of the primary particle and the index of the connection, respectively.

The molar flux at the interface between two particles in direct contact is derived from equation of mass conservation in the active particle. It is inspired by the equation proposed by Orvananos et al. [31], which is used in its more general form [3]

$$\widehat{n}_{k_1,k_2} j^{DC} = \frac{\overline{c}_{s,k_1} + \overline{c}_{s,k_2}}{2} \frac{P}{RT}(\mu_{k_2} - \mu_{k_1}).\qquad(2)$$

The rate of Li exchange between particles with indexes k_1 and k_2 is determined by their difference in chemical potential, and has an impact on the particle lithiation process during phase transformations between the Li-rich and Li-poor phase. $\overline{c}_s$ represents the average concentration of Li in active particles, whereas P represents the permeability of the direct contact surface, and can be model-driven to account for the misalignment of 1D fast diffusion channels at the interface. The intercalation molar flux of Li $j_{j,k}$ to or from the individual primary particle is, therefore, the contribution of molar flux between the particle and the electrolyte, and the molar flux between particles in direct contact weighted by the corresponding surfaces

$$j_{j,k} = \frac{1}{A_{j,k}} \left(j_{j,k}^e A_{j,k}^e + \sum_l j_{j,k,l}^{DC} A_{j,k,l}^{DC} \right).\qquad(3)$$

As the direct contact molar flux j^{DC} does not contribute to the charge

transfer between the solid and the electrolyte, it is not the part of the equation for a total molar flux at the solid-electrolyte interface, i.e. Eq. 4.

One of critical prerequisites for adequate modelling of Li exchange between particles (Eq. 2) arises from the plausible model of the chemical potential μ_{k_i}. A.3 summarises advanced and consistent scale bridging methods to calculate chemical potentials of the primary LFP particles [29] based on multi-scale sequential linking approach [29].

To comply with further objectives of the advanced modelling framework on the interaction between main and side reactions, the extended equation for the total molar flux, which is the source of transport equations in Section A.2 was derived. Hence, j^{tot} that couples transport equations – Eqs. A.1, A.3, and A.4 – and fluxes of those considered degradation reactions (Section 2.2) that contribute to transport of charge species. It is written as

$$j^{\mathrm{tot}} = j^{\mathrm{e}} + j^{\mathrm{SEI}} + j^{\mathrm{LPL}}, \tag{4}$$

where j^{e} represents charge transfer molar flux, j^{SEI} represents molar flux to the SEI layer (Section 2.2.1) and j^{LPL} represents the molar flux of metallic Li plating on the anode's active material (Section 2.2.4). Formulation of the corresponding molar fluxes of side reactions or degradation mechanisms will be elaborated in the following subsections.

For the charge transfer molar flux j^{e}, the widely adopted Butler–Volmer equation is used [23]

$$j^{\mathrm{e}} = \frac{i_0}{F} \left[\exp\left(-\frac{\alpha F}{RT} \eta^{\mathrm{e}} \right) - \exp\left(\frac{(1-\alpha)F}{RT} \eta^{\mathrm{e}} \right) \right], \tag{5}$$

where i_0 represents exchange current density (A.4), α represents charge transfer coefficient, and η^{e} represents overpotential.

Overpotential represents another parameter, where extensions need to be introduced to address the interplay between main and side reactions. Integration of the effects of considered side reactions yield the following functional dependency [28]

$$\eta^{\mathrm{e}} = (\Phi_s - \Phi_e) - U^{\mathrm{EQ}} + F \frac{\omega^{\mathrm{SEI}} \delta^{\mathrm{FILM}}}{\kappa^{\mathrm{SEI}}} \left(j^{\mathrm{e}} + j^{\mathrm{SEI}} + j^{\mathrm{LPL}} \right). \tag{6}$$

The last term in Eq. 6 represents the rise of particle overpotential because of the resistivity of the interphasial film created on the surface of active anode particles (explained in Section 2.2). Side and main reactions are thus interacting simultaneously via Eqs. 4 and 6.

2.2. Models of side reactions

Literature offers a multitude of proposed mechanisms and models in the area of the SEI growth, e.g. [11]. Due to availability of comprehensive review articles, only some important aspects related to elaboration of the chain of side reaction models will be analysed in this part of paper to preserve brevity.

To ensure high level of versatility, the proposed modelling framework is developed in the way to enable simulating the outbreak of thermal runaway in arbitrary combination of external and/or self-induced and/or battery operation as presented in Figs. 1 and 3. Therefore, models of side reactions are coupled into the causality chain originating from electrochemical, transport and heat generation phenomena.

During battery operation side reactions of SEI formation and Li-plating contribute to the growth of the interphasial film at the anode, e.g. [28]. At elevated temperatures, the thickness of the SEI layer is reduced due to exothermic SEI decomposition [32] to such an extent that parts of the graphite anode are exposed to the electrolyte. This direct contact leads to the subsequent exothermic reactions between exposed intercalated Li in the anode with the surrounding electrolyte, i. e. SEI regeneration [18]. These exothermic reactions might increase the temperature to a level promoting cathode-electrolyte reactions, e.g. [7], oxygen dissolution from active, in particular cathode, materials, e.g. [8], and electrolyte decomposition reactions [9]. After the sequence of these

reactions the temperature of the battery, in general, reaches the temperature at which it is very unlikely that thermal runaway can be avoided [18], therefore, if reactions progress to this level, this state is denoted as the outbreak of the thermal runaway.

Due to limited understanding of the safety critical side reactions, as discussed in Introduction, and due to the aim of harmonising modelling depths of models replicating side reactions, they were, in this demonstrative example, modelled with phenomenological and empirical models. Therefore, the following models, in their original or adapted version, were applied: SEI formation [28], SEI decomposition [18], SEI regeneration [18], Li-plating [28], cathode decomposition [9] and electrolyte decomposition [9]. Due to good thermal stability of the LFP material [33] and due to the fact that no long term exposure to high temperature is considered in this study the current model does not comprise metal dissolution and its transport from the cathode to the anode [8] and Fe enhanced reactions of the SEI formation [10]. Likewise, due to the fact that the capacity fading of LFP-graphite batteries is mainly ascribed to the consumption of active lithium by the inner structural deterioration of graphite anodes upon cycling [34], capacity loss relevant models of SEI formation and Li-plating will be applied at the anode. Li-plating will be considered despite the fact that fast charging at low temperatures, where Li-plating is most pronounced [35], will not be considered, as it contributes to the interphasial film thickness in particular in degraded cell featuring higher overpotentials [28]. However, due to generic structure of the proposed electrochemical, transport, and thermal modelling framework presented in Sections 2.1 and 2.3, it is easily possible to exchange all sub-models and add transport of additional species. These interaction of specific side reactions models are schematically depicted in Fig. 3. Listed models were implemented in their original or reformulated forms to ensure the consistent coupling between models of different side reaction phenomena and to ensure compliance with the particle based formulation of electrode models.

2.2.1. Solid electrolyte interphase formation

The SEI formation reaction was modelled by the Tafel equation described in reference [28]. Using the Tafel model, Li-ion flux j^{SEI} from the electrolyte to the SEI layer (introduced in the Eq. 6) can be written as

$$j^{\mathrm{SEI}} = A_0^{\mathrm{SEI}} c_{\mathrm{SURF}}^{\mathrm{EC}} \frac{1}{a^e} \exp\left(-\frac{\alpha^{\mathrm{SEI}} F}{RT} \eta^{\mathrm{SEI}} \right), \tag{7}$$

where A_0^{SEI} denotes the SEI formation reaction frequency factor and η^{SEI} is the overpotential for the SEI formation reaction at the SEI/graphite interface. The overpotential η^{SEI} can be written similarly as in Eq. 6

$$\eta^{\mathrm{SEI}} = \Phi_s - \Phi_e - U^{\mathrm{SEI}} + F \frac{\omega^{\mathrm{SEI}} \delta^{\mathrm{FILM}}}{\kappa^{\mathrm{SEI}}} \left(j^{\mathrm{e}} + j^{\mathrm{SEI}} + j^{\mathrm{LPL}} \right). \tag{8}$$

U^{SEI} denotes standard electrode potential of SEI relative to the reduction potential of metallic lithium (denoted by Li/Li$^+$ potential). κ^{SEI} represents the ionic conductivity of the interphasial layer and ω^{SEI} is the volume fraction of SEI in the film. The last term in the equation describes the change in overpotential because of the ionic resistance of the interphasial film [28]. $c_{\mathrm{SURF}}^{\mathrm{EC}}$ is the molar concentration of ethylene carbonate (EC) at the graphite surface, which depends on the rate of diffusion of EC from the electrolyte through the SEI layer. Therefore, it can be determined from the following equation [28]:

$$D^{\mathrm{EC}} \frac{c_0^{\mathrm{EC}} - c_{\mathrm{SURF}}^{\mathrm{EC}}}{\delta^{\mathrm{FILM}}} = j^{\mathrm{SEI}}, \tag{9}$$

where D^{EC} is the diffusion coefficient of EC in SEI layer, c_0^{EC} is the molar concentration of EC in electrolyte, and δ^{FILM} is the thickness of interphasial film described in Section 2.2.5.

2.2.2. Solid electrolyte interphase decomposition

The decomposition of SEI becomes significant at elevated temperatures. According to reference [36], it becomes significant above 60 °C and can be described by Arrhenius equation:

$$j^{\text{SEI}_D} = -A_f^{\text{SEI}_D} \delta^{\text{FILM}} \frac{\rho^{\text{SEI}}}{M^{\text{SEI}}} \exp\left(-\frac{E_a^{\text{SEI}_D}}{RT}\right), \tag{10}$$

where j^{SEI_D} represents the molar flux of lithium from the SEI to electrolyte because of the decomposition reaction, $A_f^{\text{SEI}_D}$ is a frequency factor in the Arrhenius equation, ρ^{SEI} and M^{SEI} are the specific density and molar mass of SEI, respectively, and $E_a^{\text{SEI}_D}$ is the activation energy of the reaction.

2.2.3. Lithium reaction with electrolyte at anode interface

At elevated temperatures, the SEI decomposition reaction overrides SEI formation [6]. The end result of such a regime is the reduction of the SEI layer thickness to an extent that parts of graphite anode are exposed to the electrolyte. Direct contact between electrolyte and lithiated graphite leads to the reaction of SEI regeneration [6], i.e. reactions between exposed intercalated Li in the anode with the surrounding electrolyte. In line with the reference [18], such a reaction can be described by an Arrhenius equation of the following form:

$$j^{\text{Li}-\text{el}} = A_f^{\text{Li}-\text{el}} c_s^{\text{SURF}} \frac{1}{a^e} \exp\left(-\frac{E_a^{\text{Li}-\text{el}}}{RT}\right) \exp\left(-\frac{\omega^{\text{SEI}} \delta^{\text{FILM}}}{\delta_0^{\text{FILM}}}\right). \tag{11}$$

Here, $j^{\text{Li}-\text{el}}$ represents the molar flux of lithium, $A_f^{\text{Li}-\text{el}}$ is a frequency factor in the Arrhenius equation, c_s^{SURF} is the surface concentration of lithium in active anode particles, $E_a^{\text{Li}-\text{el}}$ is the activation energy of the reaction, and δ_0^{FILM} is the critical thickness of interphasial film at which the Li reaction with electrolyte at the anode interface becomes significant.

2.2.4. Lithium plating

Li plating was modelled with the Tafel equation, using the approach presented in reference [28]. The lithium molar flux j^{LPL} to interphasial film because of Li plating (introduced in Eq. 6) can be calculated as:

$$j^{\text{LPL}} = \frac{i_0^{\text{LPL}}}{F} \exp\left(-\frac{\alpha^{\text{LPL}} F}{RT} \eta^{\text{LPL}}\right), \tag{12}$$

where i_0^{LPL} denotes the exchange current at Li plating formation reaction, α^{LPL} is the charge transfer coefficient, and η^{LPL} is the overpotential for the Li plating reaction. The overpotential η^{LPL} can be again written similarly as in Eq. 8

$$\eta^{\text{LPL}} = \Phi_s - \Phi_e + F \frac{\omega^{\text{SEI}} \delta^{\text{FILM}}}{\kappa^{\text{SEI}}} \left(j^e + j^{\text{SEI}} + j^{\text{LPL}}\right), \tag{13}$$

with the assumption of open circuit potential of plated Li versus Li/Li$^+$ being zero.

2.2.5. Interphasial film thickness

The interphasial film thickness time derivative is determined by the sum of all lithium fluxes in the film [28], and can be written as:

$$\frac{\partial \delta^{\text{FILM}}}{\partial t} = \frac{M^{\text{SEI}}}{2\rho^{\text{SEI}}} \left(j^{\text{SEI}} + j^{\text{SEI}_D}\right) + \frac{M^{\text{Li}}}{\rho^{\text{Li}}} j^{\text{LPL}}. \tag{14}$$

2.2.6. Electrolyte decomposition

At the elevated temperatures side reaction of electrolyte decomposition initiates. According to reference [9] this reaction can be described by the following equation:

$$R_e = \frac{dX_e}{dt} = A_e X_e \exp\left(-\frac{E_a^e}{RT}\right), \tag{15}$$

where compared to the reference [9], a dimensional quantity (volumetric number of moles) of electrolyte inside control volume i.e. X_e was used. Additionally, A_e and E_a^e represent the frequency factor and activation energy for the electrolyte decomposition, respectively. Unlike in previous section, where area specific molar fluxes are calculated, electrolyte decomposition is given as a volumetric source.

2.2.7. Cathode active material degradation

Degradation of active material and heat that is released during this side reaction in cathode is modelled by the model presented in Ref. [9]. The process of cathode degradation can be described by Arrhenius equation

$$R_{pe} = \frac{d\alpha_{\text{pe}}}{dt} = A_{\text{pe}} \alpha_{\text{pe}}^m (1 - \alpha_{\text{pe}})^m \exp\left(-\frac{E_a^{\text{pe}}}{RT}\right). \tag{16}$$

α_{pe} represents the degree of conversion of the active material of the cathode [9]. This parameter is further used in the heat generation equation at the cathode degradation reaction (Eq. 30). A_{pe} is frequency factor, E_a^{pe} is activation energy and m denotes the reaction order.

2.2.8. Loss of cyclable Lithium

Loss of the cell capacity due to the loss of cyclable lithium in degradation reactions from Sections 2.2.1, 2.2.3, 2.2.4 and 2.2.6 is calculated by integration of all molar fluxes that irreversibly consume cyclable lithium:

$$C_{\text{loss}}(t_0) = VF \int_0^{t_0} \left[a^e \left(j^{\text{SEI}} + j^{\text{LPL}} + j^{\text{Li}-\text{el}}\right) + R_e\right] dt. \tag{17}$$

$C_{\text{loss}}(t_0)$ represents the lost capacity at time t_0, a^e is volumetric active material surface density and V is volume of the cell respectively.

2.3. Thermal model

The thermal model represents one of the important building blocks of the high fidelity modelling framework (Fig. 1), as temperature decisively influences material properties and thus, the reaction rates of main and side reactions. Heat transport across the cell's components is governed by the classic heat equation

$$\rho c_p \frac{\partial T}{\partial t} = \nabla \cdot (\lambda \nabla T) + \sum_i q_i^{\text{v}}, \tag{18}$$

where ρ, c_p, and λ represent cell averaged density, specific heat, and the thermal conductivity coefficient, respectively. To properly address causal chain between main and side reactions as well as heat generation, Eq. 18 innovatively considers heat generation term due to inter primary particle transport of Li, and heat generation due to side reactions.

$\sum_i q_i^{\text{v}}$ represents the sum of individual heat sources, and can be written as:

$$\sum_i q_i^{\text{v}} = q_{\text{irreversible}}^{\text{v}} + q_{\text{reversible}}^{\text{v}} + q_{\text{degradation}}^{\text{v}} \tag{19}$$

$$q_{\text{irreversible}}^{\text{v}} = q_{\text{react}}^{\text{v}} + q_{\text{ohm}}^{\text{v}} + q_{\text{Li,ts}}^{\text{v}} \tag{20}$$

$$q_{\text{reversible}}^{\text{v}} = q_{\text{rev}}^{\text{v}} \tag{21}$$

$$q_{\text{degradation}}^{\text{v}} = q_{\text{SEI}_D}^{\text{v}} + q_{\text{Li}-\text{el}}^{\text{v}} + q_{e_D}^{\text{v}} + q_{\text{pe}}^{\text{v}} \tag{22}$$

Irreversible heat sources (Eq. 20) are attributed to three different contributions.

First, heat sources due to main reactions at the solid/electrolyte interface, which consider also contributions due to SEI growth and Li plating currents evaluated with the following equation:

$$q_{\text{react}}^{\text{v}} = a^e F \left(j^e \eta^e + j^{\text{SEI}} \eta^{\text{SEI}} + j^{\text{LPL}} \eta^{\text{LPL}}\right). \tag{23}$$

The later two contributions are considered in Eq. 23, as they contribute to transport of charge species, as addressed with Eq. 4.

Second, ohmic losses $q_{\text{ohm}}^{\text{V}}$ in the electrolyte because of electron and ion transport within the cell [37], evaluated by

$$q_{\text{ohm}}^{\text{V}} = \sigma^{\text{eff}}(\nabla\Phi_s)^2 + \kappa_e^{\text{eff}}(\nabla\Phi_e)^2 - 2\frac{\kappa_e^{\text{eff}}RT}{F}\left(1 - t_+\right)\left(1 + \frac{\partial\ln f_{\pm}}{\partial\ln c_e}\right)\nabla\left(\ln c_e\right)\nabla\Phi_e,$$ (24)

where σ^{eff} and κ_e^{eff} represent effective conductivity of solid and electrolyte phase, c_e denotes concentration of lithium inside electrolyte and $f_{\pm}$ represents an activity coefficient, determined as described in references [38,39].

Third, to ensure a consistent treatment of transport (Eq. 1) and and heat generation phenomena, an additional irreversible heat source originating from Li transport inside secondary active particles has been included, i.e. the term $q_{\text{Li,ts}}^{\text{V}}$ in Eq. 22. This contribution has been modelled with two different approaches that are consistent with the transport modelling approach.

In the case where secondary particles are modelled as homogeneous spheres, as proposed in the Newman's approach, heat source due to Li transport in active solid was modelled with the approach proposed in reference [40] that is reformulated to the form compatible with presented modelling framework in Section A.5. The end equation reads:

$$q_{k,\text{Li,ts}}^{\text{V}} = -RT\frac{D_s}{c_s}\nabla c_s\nabla c_s,$$ (25)

where c_s represents concentration of lithium in solid and D_s is diffusion coefficient of lithium in solid.

An innovative heat generation approach due to Li redistribution between primary particles in direct contact within a secondary particle, i.e. agglomerate, is derived to ensure consistency with the advanced transport modelling framework presented in Section 2.1. The resulting heat generation due to Li redistribution between the primary particle k and the neighbouring primary particles in direct contact l is modelled as

$$q_{k,\text{Li,ts}}^{\text{V}} = \sum_l a_l^{\text{DC}} j_l^{\text{DC}} \Delta\mu_l$$ (26)

and depends on the specific surface of the direct contact a^{DC}, the molar flux over the surface of the direct contact between two particles j^{DC}, and the difference in chemical potential between the two particles $\Delta\mu$.

Reversible contributions in Eq. 21 are attributed to the reaction entropy change during (de) intercalation at the cathode and anode and can be written as:

$$q_{\text{rev}}^{\text{V}} = a^e T s_e j^e,$$ (27)

where s_e represents specific entropy change per mole.

The term $q_{\text{degradation}}^{\text{V}}$ in Eq. 22 describes heat sources of various degradation side reactions. The heat contribution due to SEI decomposition and reaction of exposed intercalated Li with the surrounding electrolyte, which occur on the negative electrode, are calculated as

$$q_{\text{SEI}_D}^{\text{V}} = -a^e h_{\text{SEI}_D} j^{\text{SEI}_D}$$ (28)

and

$$q_{\text{Li-el}}^{\text{V}} = a^e h_{\text{Li-el}} j^{\text{Li-el}}$$ (29)

where h_{SEI_D} and $h_{\text{Li-el}}$ are enthalpies of reactions, and j^{SEI_D} and $j^{\text{Li-el}}$ are molar fluxes described in Section 2.2.

The third contribution $q_{\text{el}_D}^{\text{V}}$ refers to the degradation of the electrolyte at the elevated temperatures and is calculated as

$$q_{e_D}^{\text{V}} = \epsilon_e H_e M_e R_e,$$ (30)

where ϵ_e represents electrolyte porosity, H_e represents the specific heat release, M_e represents the molar mass of the electrolyte and R_e represents the reaction rate which equals the term $-\frac{dc_e}{dt}$ in the Eq. 15.

The fourth contribution q_{pe}^{V} refers to the degradation of the positive electrode and is calculated as

$$q_{\text{pe}}^{\text{V}} = (1 - \epsilon_e - \varphi_f)H_{\text{pe}}\rho_{\text{pe}}M_{\text{pe}}R_{\text{pe}},$$ (31)

where φ_f represents volume fraction of the fillers in the electrode, H_{pe} is specific heat release, ρ_{pe} is density of the positive electrode material and finally, R_{pe} represents the reaction rate defined in the Eq. 16.

The first two terms in Eq. 19 describe the irreversible and reversible contributions of the intercalation reaction to heat generation. Heat source because of SEI formation is implicitly considered in the expression for overpotential in Eq. 6.

The temperature dependency of the material properties, as for example, ionic conductivity and diffusion constants, is modelled with the Arrhenius expression

$$\Psi(T) = \Psi_{\text{ref}}\exp\left[\frac{E_a^{\Psi}}{R}\left(\frac{1}{T_{\text{ref}}} - \frac{1}{T}\right)\right],$$ (32)

where Ψ is the arbitrary temperature dependent parameter, T_{ref} is the reference temperature and E_a^{Ψ} is the corresponding activation energy, which shows the sensitivity of the parameter to the temperature [41].

The modelling framework supports both temperature and heat flux boundary conditions necessary to solve Eq. 18.

3. Results

The Results section is divided into four parts. Section 3.1 elucidates the importance of the proper virtual representation of material properties and their influence on intra-cell heat generation. Section 3.2 presents and validates functionality of capacity modelling capacity loss in normal operating conditions. This section is followed by the Section 3.3, where capability of simulating thermal runaway phenomena in battery test calorimeter is presented and validated. This section is followed by the final Section 3.4 demonstrating modelling of the coupled chain of phenomena of main transport and electrochemical reactions, side reactions and heat generation leading to the thermal runaway during battery operation.

The basis for the plausible modelling of intra-cell phenomena arises from the proper modelling of transport and electrochemical phenomena, which represents the first part of model validation of the advanced multi-scale modelling framework. This validation focuses on phenomena arising from the crystallographic structure specific properties of the LFP cathode material and material specific electrode topology, which influence the electrical output of the phase separating cathode material.

Validation was performed on a LFP/graphite cell featuring a 70 μm thick cathode, 30 μm thick separator and 55 μm thick graphite anode. Model parameters and material properties are given in Section B, where temperature dependency of selected parameters is modelled with Eq. 32. In this section results are generated using 1D computational domain presented in Fig. A.2a, where the single electrochemical cell is discretized into 25 control volumes (10-5-10 for cathode-separator-anode). Comparison between selected 1D and 2D results and reasoning of plausibility of the 1D approach to model outbreak of the thermal runaway is presented in Section A.6.

3.1. Transport and heat generation phenomena

The proposed modelling framework allows for the credible modelling of very different materials, as for example the LFP-graphite cell, while adapting intrinsic material properties and considering the proper topological representation of the electrode [3].
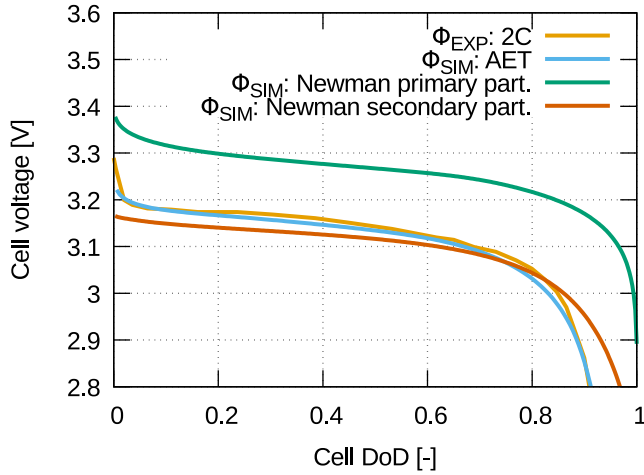
Fig. 4. Comparison of the three simulated discharge characteristics at 2C obtained with the Advanced Electrode Topology (AET), Newman primary particles and Newman secondary particles approaches to the experimentally measured discharge curve of the LFP-graphite battery obtained from [34].

To elucidate importance of proper topological representation of the electrodes, impact of various modelling depths is analysed on this challenging LFP material being characterised by its phase-separating nature and featuring fast diffusion in one dimension. The model based on the more consistent virtual representation of the electrode topology as presented in Section 2.1 is denoted as Advanced Electrode Topology (AET). To ensure a credible validation of the LFP cathode, the size of primary particles and the size and topology of secondary particles was measured experimentally with transmission electron microscope (TEM) imaging on a statistically representative number of particles [3]. Primary particles were then virtually arranged into secondary particles, that is, agglomerates, as depicted in Fig. 3. The virtual arrangement of primary particles into these secondary particles again follows the experimentally determined topologies of secondary particles (Fig. A.1). In the present simulation agglomerates were composed of approximately 50 different size classes of primary particles, whereas modelling framework support also any other selection. As presented in Section A.3.2, mass balance in anode particles is calculated with an assumption of spherical particles discretised with 6 control volumes in the radial direction.

Fig. 4 presents a good agreement between the simulated and measured voltage traces for the model relying on more consistent virtual representation of the electrode topology. As already reasoned in [3],

good agreement between the simulated and measured voltages arises from the adequacy of the model of the chemical potential of the particle and the plausibility of the virtual representation of secondary particles. Furthermore, it is also important to note that this AET model is capable of credibly virtually representing low Li utilisation at high rates, which arises from increased losses of direct Li transport between primary particles (Eq. 2). These higher losses mainly originate from particles that are positioned within agglomerates in a way that they do not have a direct contact with the electrolyte, while absence of well aligned channels for fast diffusion further increases the losses (Section 2.1).

Results of this model were benchmarked against two set of results, which feature different virtual representation of the electrode. First set of results is generated with the model featuring the same primary particle distribution as the AET model, however with the exception that primary particles are not arranged in agglomerates, but instead all of them are ideally immersed in the electrolyte in analogy with the Newman's approach, denoted as Newman primary particles. As already reported in [3], this modelling approach yields too low overpotentials and too high Li utilisation despite using the same model for the chemical potential of the particle as the AET model. As reported in [3], these discrepancy is also insensitive on the selection of the modelling approach for simulating intra-particle diffusion, as results are nearly identical when using spherical Fickian diffusion and the zero dimensional (0D) particle approach due to very short characteristic times for diffusion is such small primary particles [42]. The discrepancy to the experimental data thus expectedly arises from inappropriate topological representation of the electrode yielding too large solid electrolyte-area and very short diffusion paths as well as from inability of this modelling approach to virtually replicate hardly accessible vacancy or Li sites in particles that in real electrode do not have a direct contact with the electrolyte (Fig. A.1). Due to these deficiencies, this modelling approach will thus not be further analysed in the paper.

Therefore, this paper additionally analyses results of a second modelling approach, where cathode is virtually represented by the spherical particles, which now, apparently more realistically, represent secondary particles, i.e. agglomerates, immersed in the electrolyte, denoted as Newman secondary particles. These agglomerates are represented as spherical particles where Li transport is modelled via Fickian diffusion (Eq. A.11 following Newman's approach) and featuring diameters that ensure the same volume of agglomerates as in the AET case. Analogue to anode particles, these spherical particles are discretised with 6 control volumes in the radial direction. As discernible from Fig. 4 these results feature smaller deviations compared to the experimental results, however they feature significant qualitative model approach driven deviations. In the first part of the discharge curve this modelling
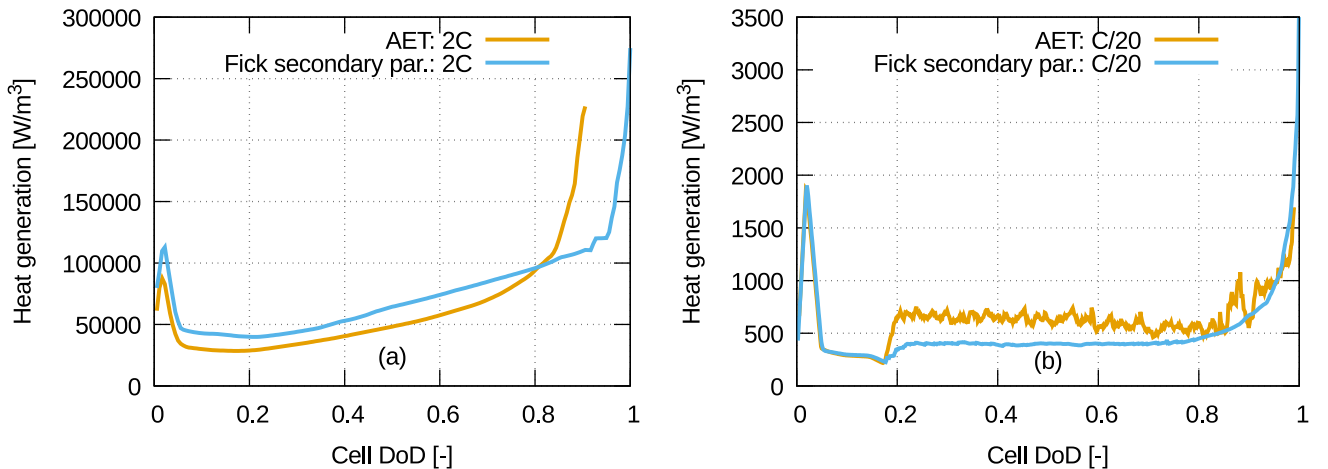
Fig. 5. Comparison of the total heat generation in the cathode between AET and Newman secondary particles approaches for (a) higher 2C rate and (b) lower C/20 rate. Significant differences in C/20 rate can clearly be related to the high inter-particle fluxes for the LFP material shown on Fig. 6b.
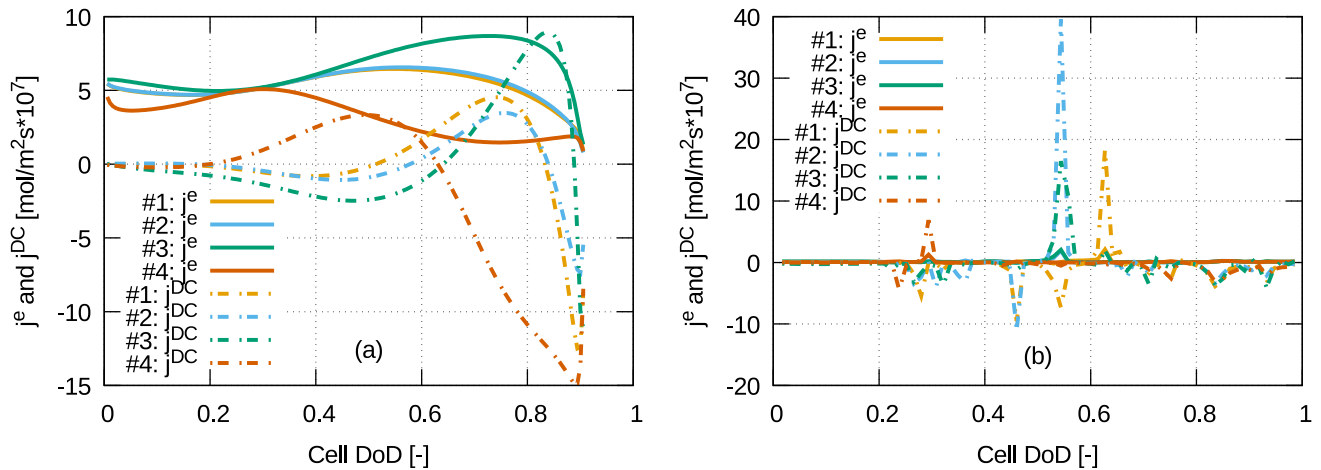
Fig. 6. Molar flux j^e and j^{DC} at 4 representative particles for (a) higher 2C rate and (b) lower C/20 rate for the AET approach.

approach features lower voltage, which is mainly the consequence of lower active surface area, since highly non-spherical LFP agglomerates (Fig. A.1) feature larger specific area than spherical particles. However, the discrepancy in the voltage trend reverses toward the end of the discharge curve. This is the consequence of application of homogeneous particles obeying Fickian diffusion to model the LFP material. This deficiency, similarly as for the Newman primary particles case, arises from the inability of this modelling approach to virtually replicate hardly accessible vacancy or Li sites in particles that in real electrode do not have a direct contact with the electrolyte. Absence of this LFP electrode topology specific functionality namely enables filling nearly all vacancy sites with Li atoms at much lower overpotential compared to the real systems and compared to more adequate virtual representation of the LFP electrode in the AET case. Due to better agreement to experimental results and thus due to the fact that this modelling approach might be considered as still acceptable from the voltage-capacity modelling point of view, this modelling approach will be further analysed in this paper.

Fig. 5 shows the impact of the modelling depth for modelling transport phenomena in cathode on the heat generation. To further complement analysis in Fig. 5, Fig. 6 presents molar fluxes of Li exchanged to the electrolyte and between the primary particles for the AET case, while for the case of Newman secondary particles all Li is exchanged with the electrolyte and heat generation due to diffusion in active material is modelled as presented in A.5. Fig. 5a shows that at high rates heat generation is of comparable magnitude for both cases in the initial part of the DoD range despite differences in topologies of secondary particles. This can be reasoned by the fact that the same amount of Li is intercalated, whereas heat generation due to small molar fluxes of Li exchange between particles in direct contact in the AET case (Fig. 6a) is overcompensated by the higher overpotential of the surface reaction due to smaller surface area of agglomerates in the case of Newman secondary particles. Unlike, heat generation of the AET case increases towards the end of the DoD range due to larger molar fluxes of Li exchange between particles in direct contact (Fig. 6a), which is mainly the consequence of lithiation of larger particles that feature reduced or negligible area in the contact with the electrolyte.

Likewise, Fig. 5b shows that at low currents heat generation is significantly higher in wide range of intermediate DoDs, within spinodal regions of the chemical potential [26], for the AET case. This is, as presented in Fig. 6b, reasoned by the inter-particle Li redistribution, because of the so-called particle-by-particle lithiation of phase separated particles at lower local overpotentials and thus at low currents being well documented in relevant literature [26,43]. Capability, of the proposed advanced modelling framework to replicate this, for a continuum scale very challenging particle-by-particle mode of lithiation [3],

confirms enhanced consistency to mesoscopic phenomena in batteries. Therefore, consistent, mesoscale inspired, representation of the electrode topology and consistent scale bridging methods to calculate chemical potentials of the primary LFP, provide a credible basis for extensions with irreversible heat source originating from Li transport inside secondary active particles (Eq. 26).

3.2. Capacity loss

This section presents the simulation results of the capacity loss. As reasoned in Section 2.2, capacity loss due to SEI formation and Li-plating are considered in the normal operating range to the battery. Fig. 7a shows comparison between simulated and measured discharge curves after different number of cycles at 2C rate and temperature of 25 °C, where measured data are taken from [34]. Simulated results were generated with the AET model of the cathode. Results in Fig. 7a are compared considering measured loss of capacity, which was transformed into the film thickness as proposed in [9] and used as initial condition of the model. Good agreement between various discharge curves confirms that transport and electrochemical model is capable of adequately replication performance of degraded cells, which indicated that degradation phenomena related increase of overpotentials and loss of capacity can be plausibly replicated by the model.

Good agreement presented in Fig. 7a is a prerequisite for plausible modelling of capacity loss due to SEI growth and Li-plating, which are driven by concentration and potential fields. Fig. 7b thus confirms capability of the modelling framework to plausibly predict capacity loss over multiple cycles, whereby simulation results were generated by simulation the entire 800 cycles. Complemented by Fig. 7c, which displays a well-known square root trend in SEI growth [44], it indicates that Li-plating becomes more pronounced for more degraded cell, which is in-line with findings in the literature, e.g. [28]. This phenomenon is attributed to more pronounced rate of Li-plating due to decrease of anode porosity associated with SEI growth, which aggravates the local electrolyte potential gradient in the anode [28]. Furthermore, Fig. 7c clearly shows that SEI growth is more pronounced near the separator, which is in-line with [28]. These results further support importance of considering spatially resolved degradation phenomena coupled to the electrochemical model when virtually assessing degradation phenomena during battery operation.

3.3. Thermal runaway in battery test calorimeter

This section focuses on the validation of the capability to model thermal runaway in battery test calorimeter (BTC) using experimental data published by [9]. Fig. 8 presents results of the thermal runaway test
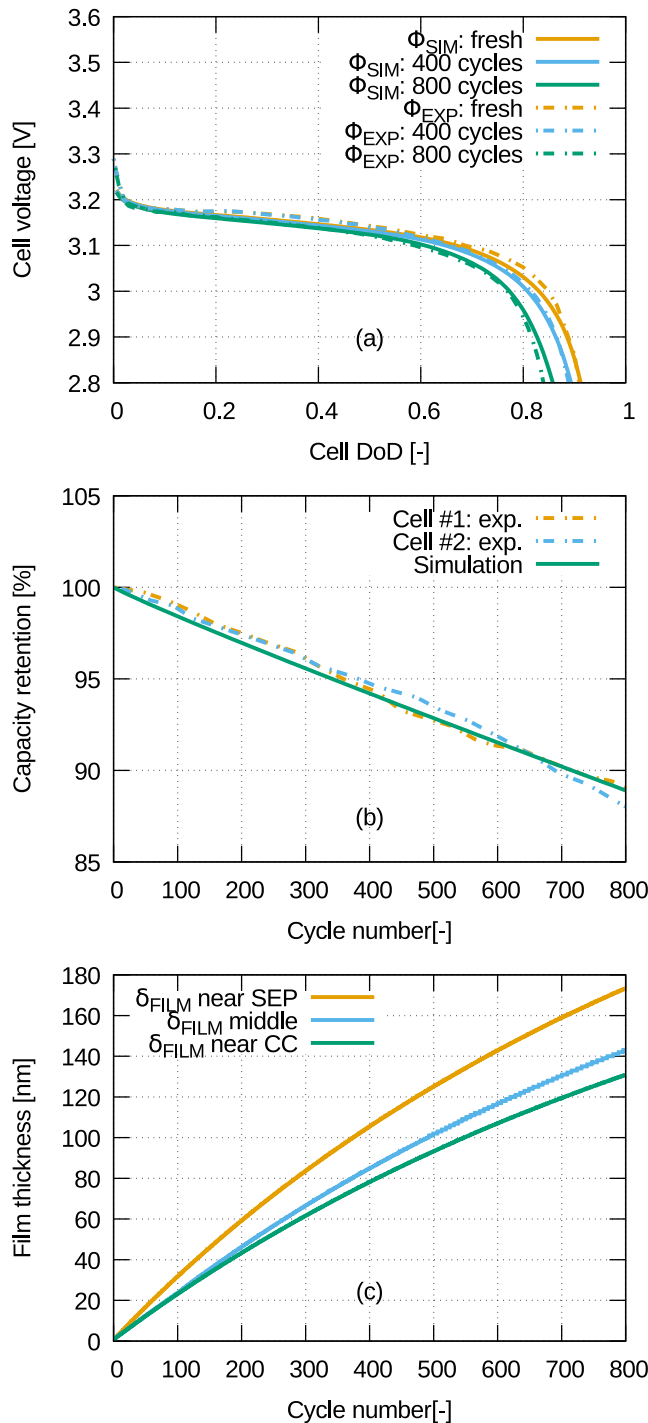
Fig. 8. Comparison of simulated and measured [9] average surface temperature of a fresh battery cell during thermal runaway test in BTC.

spatial position in the entire battery cell a lumped thermal mass approaches, as presented in the next section, or full 3D cell resolved models, e.g. [46], can be applied. Results in Fig. 8 were simulated applying the identical parameters as proposed in [9], adapted to the formulation of equations presented in Section 2.2. Fig. 8 shows that the applied model is capable of credibly simulating the measured trend of the complex chain of phenomena resulting in the outbreak of thermal runaway. Similarly, as in the publication of [9], all partial simulated trends do not feature exactly the same gradients as the measured ones, however it was decided to use the same model parameters as published in the original publication [9] rather than fitting the model with the sole aim to match all these partial trends.

3.4. Thermal runaway during battery operation

This section demonstrates the need to preserve consistency to lower scales when modelling coupled chain of phenomena of main transport and electrochemical reactions, side reactions and heat generation (Figs. 1 and 3) leading to the outbreak of the thermal runaway during battery operation. This demonstration is based on the modelling framework presented in Section 2 and validated in previous sections. Published literature does, to the best of authors knowledge, not provide sufficiently thoroughly documented report of the thermal runaway during battery operation including all required input parameters to validate this case. However, due to previous thorough validation of specific models in previous sections, this virtual demonstration relies of sufficiently credible basis to demonstrate importance of multi-scale modelling approaches when assessing coupled phenomena in batteries.

Figs. 9 and 10 present results of two selected demonstration cases. As modern batteries, in particular the LFP-graphite cells simulated in this paper, are, in general, very safe, it is challenging to select proper demonstration cases, where battery enters into thermal runaway due to mechanisms presented in Section 2.2, without simulating collapse of the separator, which was avoided to ensure demonstration of interactions between main and side reaction as well as heat generation. Therefore, Fig. 9 shows high C rate case with moderately good bottom cooling, represented with heat transfer coefficient of 50 W/m²K, of large prismatic cell featuring height of 20 cm. Unlike in the near adiabatic case analysed in Section 3.3 cell cannot be assumed as isothermal in these conditions. It is obvious that such long term simulations with coupled models of high fidelity and with full 3D resolution cannot be performed in reasonable time. Therefore, a simplified lumped thermal approach, where cell is divided into two computational domains, was applied in this analysis. The cell was thus divided in the upper, hotter, part featuring 25% of the cell height, and lower, cooler, part featuring 75% of

Fig. 7. (a) Comparison of simulated and measured discharge curves after different number of cycles at 2C rate and temperature of 25 °C, (b) comparison of simulated and measured discharge capacity loss and (c) simulated SEI thickness as a function of number of cycles and position in the negative electrode. Measured results obtained from [34].

according to the well-known HWS (heat, wait, search) method [9]. To ensure as credible validation of the results, simulated procedure fully followed the experimental one. This means that in the simulation the same amount of external heat at the same times was supplied to the cell as in the experiment. As Biot number is, in general, very small in batteries [45], a single electrochemical cell can be, in such adiabatic demonstration studies, applied as credible representation of the entire battery cell. Whereas, if specific phenomena are analysed on the level of
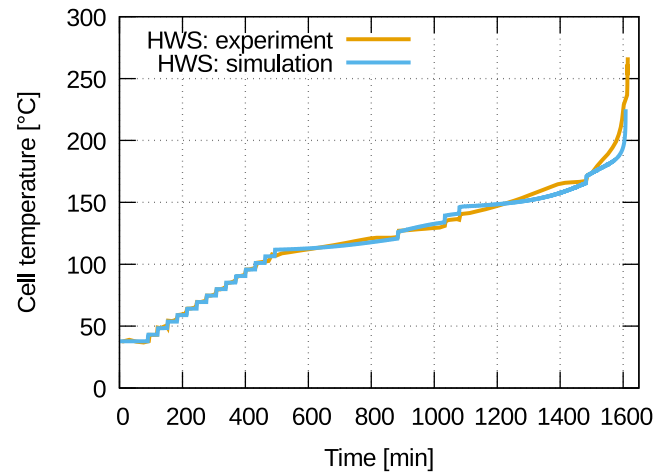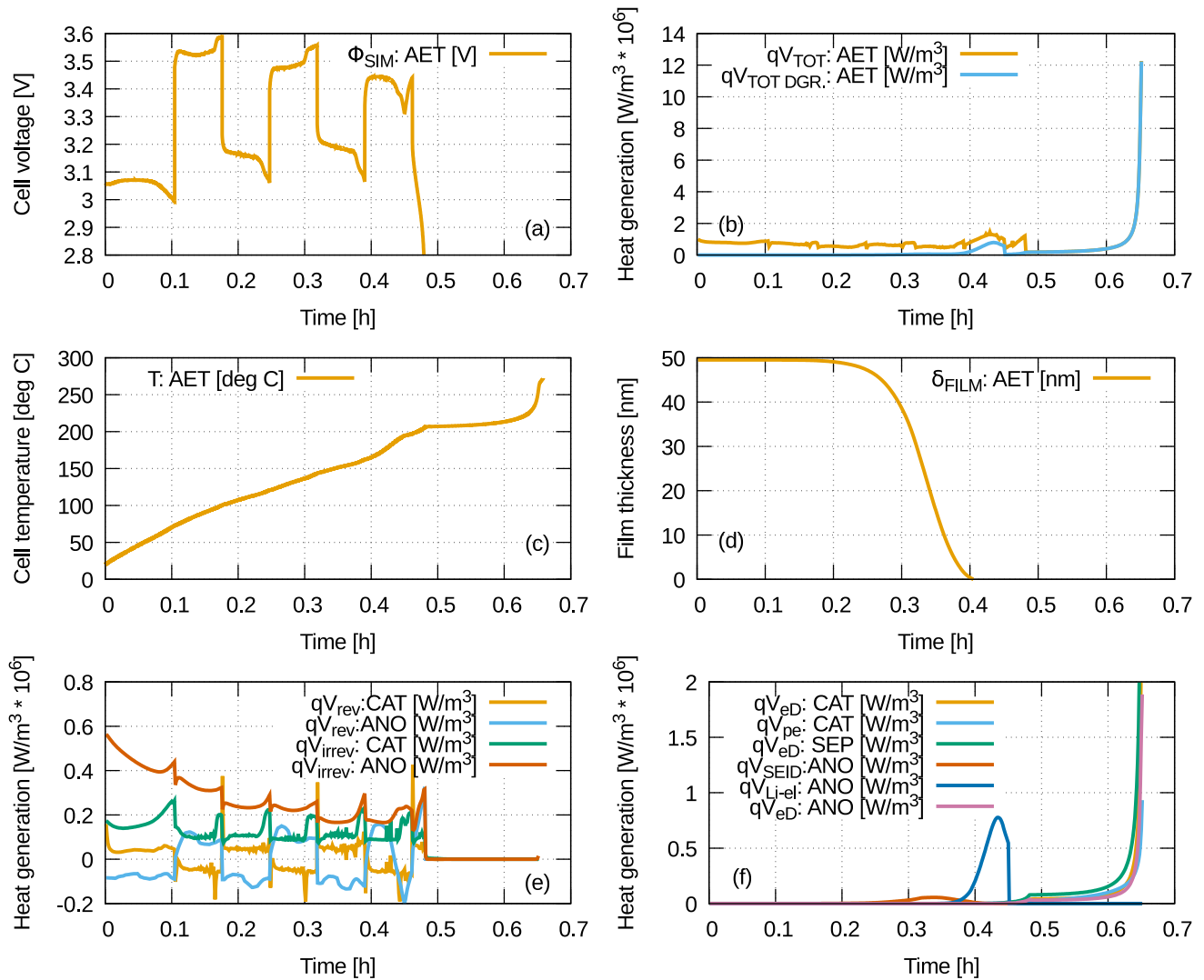
Fig. 9. Cycling of a bottom cooled prismatic cell at ±7C rate: (a) cell voltage, (b) heat generation and total heat generation related to side reactions, (c) cell temperature, (d) film thickness on the particle closest to the separator, (e) reversible and irreversible heat generation and (f) heat generation due to the individual degradation mechanisms.

the cell height. This division of the battery cell to two different computational domains enables simple virtual representation of temperature variation within the cell and consideration of inertial effects. Certainly, modelling framework is capable of supporting arbitrary number of different computational domains, however at the expense of increased computational time. Fig. 9 shows results of the upper, hotter, part of the cell, which is more prone to the thermal runaway. Unlike Fig. 9, Fig. 10 presents a very controlled numerical experiment that enables clearly exposing modelling approach specific differences by using adiabatic boundary conditions. Besides being a numerically favourable example for comparing different models, this case might mimic a limiting case of a very poorly cooled battery. In both cases, the SEI thickness was initialised with 50 nm to ensure clarity of figures by avoiding excessively long time axes. This corresponds to a degraded cell, which is a realistic candidate for entering into the thermal runaway due to SEI decomposition [47,48].

Fig. 9 shows an exemplary case of a high power application, where cell is cycled at ±7C with a relatively poor cooling due to high thermal stability of LFP-graphite cells, as discussed above. This case was modelled with the AET model as at high rates relative differences in transport specific heat generation are less pronounced (Section 3.1).

Fig. 9e clearly shows that at high currents a lot of heat is generated

already when battery operates at normal temperatures due to high irreversible heat generation. Fig. 9e also shows that maximum values of reversible contributions are relatively high at such high currents when compared to the irreversible contribution. In this context it needs to be considered that reversible sources have different signs at the cathode and at the anode (Fig. 9e), which reduces their impact on the temperature history of the cell, in addition to their reversible nature. Due to this initial high heat generation, battery temperature rises relatively fast (Fig.9c) and reaches temperature of SEI decomposition (Fig.9d). This exothermic reaction further releases a moderate amount of heat compared to other degradation side reactions (Fig. 9), however SEI decomposition represents a prerequisite for subsequent side reactions.

SEI thinning namely make possible another exothermic reaction between exposed intercalated Li in the anode with the surrounding electrolyte, i.e. SEI regeneration. In this demonstration case, it is assumed that overheating event is not detected by the battery management system (BMS), which might be reasoned by for example insufficient number of temperature sensors. Therefore, current is not reduced or cut, promoting further cell heat up. Hence, after the SEI decomposes its thinning enable the direct contact of anode material and electrolyte resulting in SEI regeneration at high temperatures, which is associated with high heat generation (Eq. 29 and Fig. 9f). This is in-line
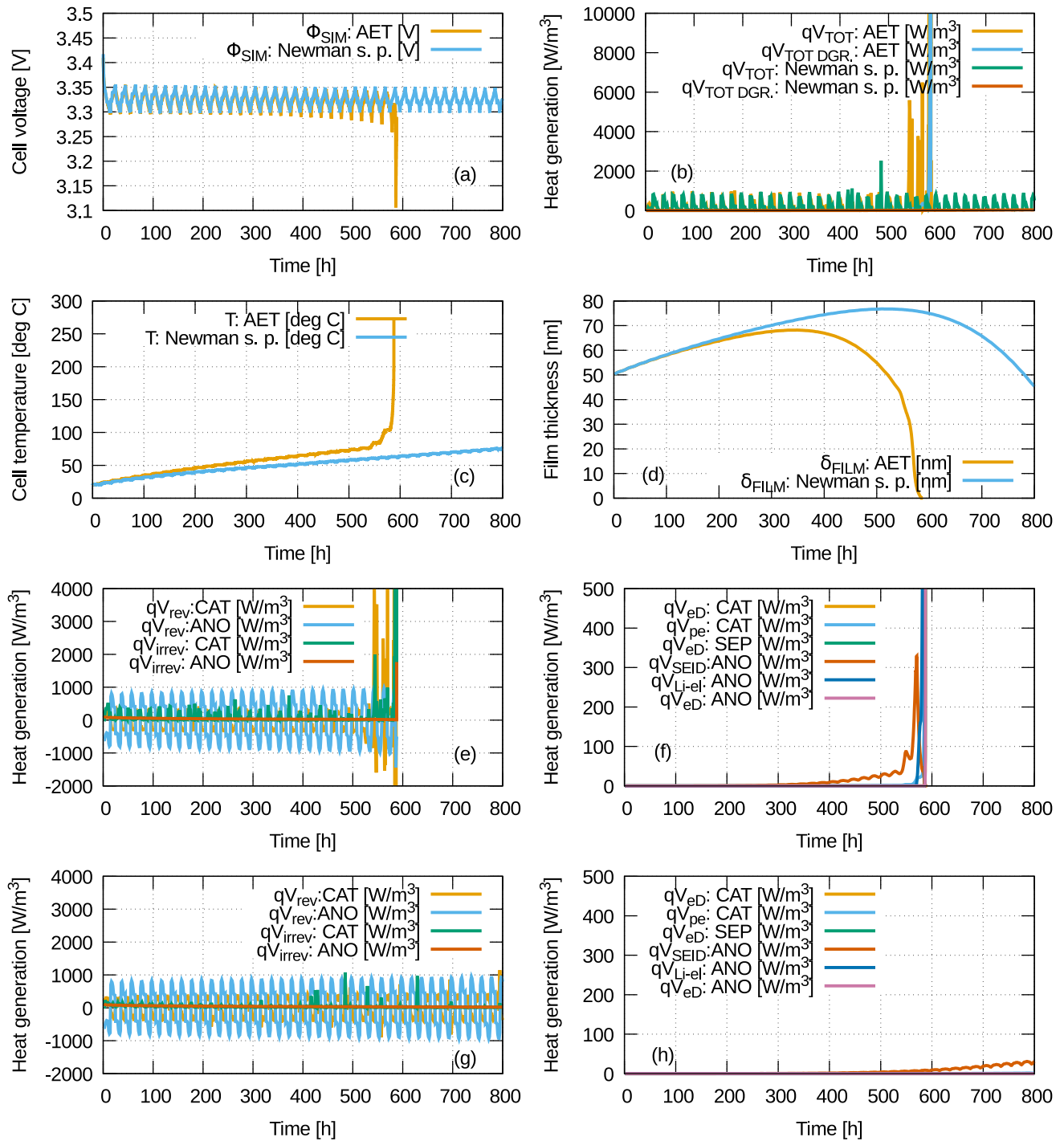
Fig. 10. Comparison of results related to adiabatic cell cycling at $\pm$C/20 rate for the AET and the Newman secondary particles approach: (a) cell voltage, (b) heat generation and total heat generation related to side reactions, (c) cell temperature, (d) film thickness on the particle closest to the separator, (e) and (g) reversible and irreversible heat generation for AET and Newman secondary particles approach, respectively, (f) and (h) heat generation related due to the individual degradation mechanisms for AET and Newman secondary particles approach, respectively.

with the experimental results of reference [18]. This results in a higher rate of temperature rise around 0.45 h (Fig. 9c).

Furthermore, coupled simulation approach also clearly indicates the cross-influence of SEI regeneration and the voltage profile (Fig. 9a). SEI regeneration is namely associated with significant loss of cyclable Li thus resulting in loss of cell capacity and lower cell voltage. Lower cell voltage namely originates from the higher overpotentials caused by additional passivating layers and increased transport losses both further promoting the rate of heat generation. This voltage drop is more likely to

the detected by the BMS and thus in agreement with functionally of real BMSs the current is cut after a significant voltage drop.

During this heating up procedure mainly driven by SEI regeneration, a threshold for degradation of active cathode material, e.g. [9], is reached resulting in a further heat release (Fig. 9f). This heat release is relatively moderate due to high thermal stability of the LFP material. These results and the underlying models clearly demonstrates the capability of the modelling framework to virtually asses wide variety of materials by only changing their material specific parameters. These

cathode degradation reactions are followed by exothermic reactions of electrolyte decomposition, e.g. [9], that feature even higher rate of heat release thus further increasing the temperature of the cell and thus clearly indicating the outbreak of the thermal runaway (Fig. 9).

As announced, Fig. 10 shows an example of an adiabatic low power (±C/20) cycling to presents a very controlled numerical experiment that enables clearly exposing modelling approach specific differences between the AET and Newman secondary particle approach. To preserve brevity of explanation, phenomena highlighted when analysing Fig. 9 will not be repeated. Fig. 10e and g, similarly as in the previous case, show higher maximum values of reversible contributions, when compared to the irreversible contribution to the total heat generation (Fig. 10b) for both modelling approaches. This is further reasoned by low currents. While, as stated reversible sources have different signs at the cathode and at the anode (Fig. 10e and g), proper modelling of transport properties and associated irreversible heat losses again significantly influences the results of this coupled chain of phenomena.

Therefore, analysis originate from the nanoscale of primary particles. LFP material, owing to its phase-separating nature, is, at low rates, characterised by a small active particle population [49] associated with the particle-by-particle lithiation [26]. This increases heat generation due to Li redistribution between particles as analysed in Section 3.1. As analysed in Section 3.1, it is obvious that higher transport driven heat generation of the AET case initiates the chain of phenomena resulting in the outbreak of the thermal runaway much earlier compared to the model relying on Newman secondary particles. This is a clear example of the cross-talk between the anode and the cathode and cross-influence of multiple coupled phenomena. Higher material specific transport losses at the cathode namely generate more irreversible heat Fig. 10e, which expectedly results in higher cell temperature Fig. 10c. This cathode induced phenomena consequently favours higher rate of exothermic SEI decomposition reactions (Fig. 10d) being prerequisite for SEI regeneration releasing even more heat (Fig. 10f). Resultantly, anode heat generation further raises the temperature to the level provoking degradation of active cathode material and electrolyte decomposition. Furthermore, Fig. 10a clearly shows the impact of loss of cyclable Li on battery performance (Section 2.2.8). Fig. 10a namely clearly presents decreasing voltage of the AET cell due to pronounced loss of cyclable Li, which further increases heat generation and leads to collapse of the battery voltage after high amount of Li was lost.

3.5. Computational times

Computational time largely depends on nature of the equation system to be solved but also on the computational mesh, integration time steps and the applied solver. Implicit Euler method was used to solve equation system presented in Fig. 3, which means that computational mesh influences the size of the Jacobian matrix. In the present approach, Newton–Raphson method was used to solve nonlinear systems of equations (ref [50]), whereas application of more sophisticated solvers could result in further reduction of computational times. Using a single core of a 4.7 GHz processor, real-Time (RT) factors, defined as the computational time divided by the physical time, for the 1D model using 25 control volumes at the time-step of 1 ms or frequency of 1 kHz equals 11.8, whereas at 1 s or frequency of 1 Hz, where model still ensures stable and numerically converged results, RT factor equals 0.012. For comparison, RT factor on the 1D mesh with 9 control volumes (3-3-3 for cathode-separator-anode) and identical model settings features RT factor of 0.75 at 1 ms or 1 kHz.

4. Discussion

The proposed modelling framework significantly extends previous multi-scaling approaches by establishing a consistent link from crystallographic structure specific properties of the material and material specific electrode topology over side reactions and heat generation to the outbreak of thermal runaway. All models are coupled on the continuum scale, while the current version of the model focused on introducing high level of consistent to phenomena in real batteries in terms of transport and heat generation phenomena. Consistency to lower scales is preserved by mesoscale inspired, topological representation of electrode reflected also through an advanced and consistent scale bridging methods to calculate chemical potentials of the primary LFP particles. Its generic architecture thus provides a promising basis for further extensions, which can comprise also future, even more consistent, models of the entire chain of side reactions resulting in the outbreak of the thermal runaway.

Presented results clearly confirm the hypothesis that nanoscopic transport phenomena and resulting heat generation decisively influence the entire chain of mechanisms that can lead to the outbreak of the thermal runaway. These results further indicate the importance of plausibly modelling the entire chain of phenomena when assessing these complex yet very realistic use cases of outbreak of the thermal runaway during battery cycling. Safety analyses during battery operation are namely decisive for proper selection of cells, their assembly into the modules and packs including selection of the type and topological layout of the cooling concepts as well as development of functionalities of the BMS according to the intended use of the batteries including their duty cycles and ambient conditions. It is far beyond the scope of this paper to demonstrate all these functionalities, whereas Fig. 1 clearly presents interactions of the core objective of this paper, being an advanced multi-scale battery modelling framework that establishes a consistent causal chain, to all relevant domains.

As presented in [3], the electrochemical and transport model are capable of modelling different electrode materials, which comprises also topological characteristics of particles. The thermal model is formulated in a generic manner and can easily be transferred to other electrode materials. Expectedly, models of side reactions, which are, in general, material specific, impose the biggest challenges due to their very limited or even not applicable transferability and not yet fully revealed cause and effect relations. These topics are currently under investigation in multiple projects. One of such projects, where authors of this paper are engaged, is also a large EU-funded project BIG-MAP under grant agreement No 957189 [51] within Battery 2030+ initiative focusing on developing the scientific and technological building blocks and models for accelerated battery discovery.

5. Conclusions

To push the boundaries of multi-scale modelling approaches, this paper proposes an advanced multi-scale battery modelling framework that establishes a consistent causal chain of main reactions, heat generation and transfer as well as side reactions relevant for modelling the outbreak of thermal runaway. Modelling framework is capable of delivering spatially and temporarily resolved results while achieving computational times that enable efficiently support of long-term degradation analyses. The developed multi-scale battery modelling framework covering multiple intertwined processes is innovative applied to model outbreak of the thermal runaway during battery cycling.

Presented results intuitively yet insightfully elucidate the entire chain of phenomena from electric and thermal boundary conditions, over cell design and properties of applied materials to solid electrolyte interphase growth, its decomposition and subsequent side reactions at the anode, cathode and the electrolyte that can lead to the outbreak of the thermal runaway. These results confirm hypothesis that nanoscopic transport phenomena and resulting heat generation decisively influence the entire chain of mechanisms that can lead to the outbreak of the thermal runaway. Besides being capable of modelling multiple performance and degradation relevant intra-cell phenomena illustrative results demonstrate the importance of the cross-talk between the anode and the cathode via several interlaced cross-influences.

Proposed modelling framework is thus applicable for virtual support of enhanced cell designs with existing materials and for exploring performances and degradation as well as safety relevant phenomena in high fidelity simulation tool capable of interaction with all relevant domains. This enables unprecedented safety analyses in transient operating conditions. This makes it possible to assess the interactions between different domains and optimise domains according to the intended application already very early in the development phase. Therefore, the proposed methodology significantly contributes to more accurate virtual prototyping, since it enables more efficient frontloading and allows for approaching engineering limits with higher certainty.

CRediT authorship contribution statement

Tomaž Katrašnik: Conceptualization, Methodology, Data curation, Writing - original draft, Writing - review & editing, Visualization, Supervision, Funding acquisition. **Igor Mele:** Software, Validation, Data curation, Writing - review & editing, Visualization. **Klemen Zelič:** Software, Data Curation, Writing - Review & Editing, Visualization.

Declaration of Competing Interest

The authors declare that they have no known competing financial interests or personal relationships that could have appeared to influence the work reported in this paper.

Acknowledgements

Appendix A

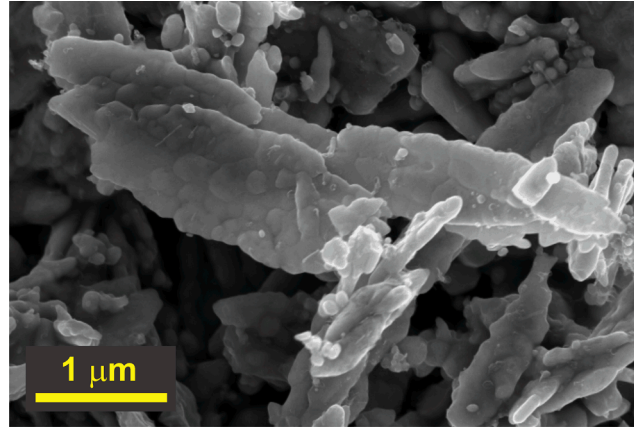### A.1. LFP cathode material

Fig. A.1. SEM image of a pristine commercial LFP cathode material. Reprinted from [3].

.

A.2. Basic electrochemical equations

The governing equations for the spatially and temporally resolved concentration and potential fields are inspired by Newman's approach [22] and porous electrode theory [52], while they are formulated and implemented in a way to ensure full compatibility with the electrode an approach relying on virtual creation of agglomerates from primary particles presented in Section 2.1.

The basic governing equations comprise the following equations, which are extended in a way to consider loss of cyclable Li due to electrolyte decomposition (Section 2.2.6). The concentration of ionic species in a binary electrolyte solution is governed by the following material balance equation

$$\frac{\partial(\epsilon_e c_e)}{\partial t} = \nabla \cdot \left(D_e^{\text{eff}} \nabla c_e \right) + a^e (1 - t_+) j^{\text{tot}} - R_e, \tag{A.1}$$

where ϵ_e represents local electrode porosity, $D_e^{\text{eff}} \nabla c_e$ represents the flux of ionic species with the effective diffusion constant evaluated from the Bruggeman relation $D_e^{\text{eff}} = D_e \epsilon_e^{\text{brugg}}$ [53,54], whereas t_+ and a^e represent the transference number and specific active surface exposed to the electrolyte, respectively, and finally, R_e represents the reaction rate due to electrolyte decomposition which is evaluated in the Eq. 15.

Porous electrode theory is based on the assumption of electro-neutrality [55] modelled as

$$\nabla \cdot i_e + \nabla \cdot i_s = 0, \tag{A.2}$$

where i_e and i_s represent liquid-phase current density and solid phase current density, respectively.

Liquid-phase potential Φ_e is governed by charge leaving or entering the liquid phase, and can be written as

$$\nabla \cdot i_e = \nabla \cdot \left(\kappa_e^{\text{eff}} \nabla \Phi_e - 2 \frac{\kappa_e^{\text{eff}} RT}{F} (1 - t_+) \left(1 + \frac{\partial \ln f_\pm}{\partial \ln c_e} \right) \nabla \ln c_e \right) = a^e F j^{\text{tot}}, \tag{A.3}$$

where κ^{eff} represents the effective liquid-phase conductivity evaluated from the Bruggeman relation $\kappa_e^{\text{eff}} = \kappa_e \in^{\text{brugg}}$ and $f_\pm$ represents the activity coefficient [38].

As in Eq. A.3, the solid phase potential Φ_s is governed by the charge leaving or entering the solid phase, and can be written in the form of Ohmic law as

$$\nabla \cdot i_s = \nabla \cdot \left(\sigma^{\text{eff}} \nabla \Phi_s \right) = -a^e F j^{\text{tot}}. \tag{A.4}$$

Effective solid phase conductivity σ^{eff} is calculated as $\sigma^{\text{eff}} = \sigma(1 - \in -\varphi^{V,\text{b+cf}})$, where $\varphi^{V,\text{b+cf}}$ represents volume fraction of binder and conductive filler combined. Parameters for the electrochemical and transport model are presented in Tables B.1 and B.2.

A.3. Equilibrium solid potentials and transport in active material

A.3.1. LFP cathode
U^{EQ} represents the equilibrium solid potential defined as

$$U^{\text{EQ}}(x) = U^0 - \frac{\mu(x)}{F}, \tag{A.5}$$

where U^0 is the standard equilibrium potential of the active material and μ represents the equilibrium chemical potential of an individual primary particle dependent on the filling fraction $x = \frac{c_s}{c_s^{\text{max}}}$. Proper determination of μ via a multi-scaling approach that provides consistent interrelation to lower scales and thus increases modelling fidelity of the cathode (elaborated in [29,30,3]) represents another merit of the proposed modelling framework.

Equilibrium chemical potential is inherently linked to the lithiation level of a particle and thus to the mass conservation in the active particle, which can, in its most general form, be written as

$$\frac{\partial c_s}{\partial t} = \nabla \cdot \left(\frac{D_s c_s}{RT} \nabla \mu \right), \tag{A.6}$$

where c_s represents concentration of Li in solid and D_s represents the diffusion constant in the solid.

The applied modern LFP cathode material features primary particles in the size range of 100 nm with fast diffusion in a 010 crystallographic direction [56,57] and thus the characteristic times for diffusion are significantly shorter than the (dis) charge time of the battery [42,30]. Originating from Eq. A.6 and considering the aforementioned specifics of the material and notation from Eq. 3, the mass conservation equation in cathode particles is calculated as [29,30,3]

$$\frac{\partial \overline{c}_s}{\partial t} = (a^e + \sum_l a^{\text{DC}}) j_{j,k}, \tag{A.7}$$

where $\overline{c}$ represents the average molar concentration in active particle and $j_{j,k}^{\text{tot}}$ is total molar flux across the particle surface defined in Eq. 3.

Averaged chemical potential μ that governs the molar flux $j_{j,k}^{\text{tot}}$ in Eq. A.7, as defined in Eqs. 5, 6, A.5 and 2 can be explicitly written in two different limits that were used in presented simulations. Low current limit averaged chemical potential reads:

$$\overline{\mu}_L = \mu_0 + \begin{cases} RT \ln \left(\frac{\overline{c}_s}{c_s^{\text{max}} - \overline{c}_s} \right) + \Omega \left(1 - \frac{2\overline{c}_s}{c_s^{\text{max}}} \right); & \overline{c}_s \quad \text{under first spinodal point} \\ 0; & \overline{c}_s \quad \text{between spinodal points} \\ RT \ln \left(\frac{\overline{c}_s}{c_s^{\text{max}} - \overline{c}_s} \right) + \Omega \left(1 - \frac{2\overline{c}_s}{c_s^{\text{max}}} \right); & \overline{c}_s \quad \text{above second spinodal point} \end{cases} \tag{A.8}$$

In the high current limit, the chemical potential reads:

$$\mu(x) = RT \ln \left(\frac{\overline{c}_s}{c_s^{\text{max}} - \overline{c}_s} \right) + \Omega \left(1 - \frac{2\overline{c}_s}{c_s^{\text{max}}} \right). \tag{A.9}$$

Ω represents regular solution parameter. Particle size dependant Ω was used in the proposed model where relation between Ω and particle size L is governed by the equation:

$$\frac{-31.4435 \, RT \, \text{nm}}{L} + 1.42925 \, RT = \sqrt{\Omega(\Omega - 2)} + \ln \left(\Omega - \sqrt{\Omega(\Omega - 2)} - 1 \right). \tag{A.10}$$

Detailed justifications and derivations of relations in Eqs. A.8, A.9 and A.10 are provided in the reference [30].

A.3.2. Graphite anode
Mass balance in anode particles is calculated with an assumption of spherical particles and a constant isotropic diffusion coefficient in the following

widely applied diffusion equation, for example, in references [23,41]:

$$\frac{\partial c_s}{\partial t} = D_s \frac{1}{r^2} \frac{\partial}{\partial r}\left(r^2 \frac{\partial c_s}{\partial r}\right). \tag{A.11}$$

There have already been some insightful attempts to model graphite's chemical potential mechanistically, e.g. [58,59], however, as graphite is not subject to such a pronounced inter-particle Li redistribution and as these models still feature some deficiencies in modelling open-circuit voltage potential in the whole range of Li concentration [58], its potential is modelled as

$$U^{\mathrm{EQ}}(x) = U^0(x), \tag{A.12}$$

where $U^0(x)$ is usually fitted to the experimental data.

A.4. Exchange current density

The exchange current density i_0 in Eq. 5, applied at the anode side, can be written as

$$i_0 = i_0' \sqrt{\frac{c_e}{c_e^{\mathrm{ref}}} x(1-x)}, \tag{A.13}$$

where c_e^{ref} represents the reference concentration of Li-salt in the electrolyte. The exchange current density i_0 in Eq. 5 at the cathode side is derived from regular solution theory [60] and can be written as

$$i_0 = i_0' \sqrt{\frac{c_e}{c_e^{\mathrm{ref}}} x(1-x) \exp\left(\frac{\Omega}{RT}(1-2x)\right)}, \tag{A.14}$$

where Ω represents the regular solution parameter [29,42].

A.5. Heat generation due to diffusion in active material

Equation for the heat that is generated due to the Li diffusion flux in the active electrode material 26 was derived from the equation published in [40]. Reference [40] offers the expression for total generated heat during the lithium diffusion in active solid that reads:

$$q_{\mathrm{Li,ts}} = -F \frac{\partial U_0}{\partial c_s} \frac{\vec{N}^2}{D_s}, \tag{A.15}$$

where z_+ represent charge number of diffusion specie, F is Faraday constant, U_0 equilibrium voltage, c concentration of diffusion specie in solid, $\vec{N}_+$ is diffusion flux and D_s is diffusion coefficient. By taking into account the relationships:

$$\mu = FU_0, \tag{A.16}$$

$$\nabla \mu = \frac{\partial \mu}{\partial c} \nabla c = \frac{1}{c_s} \nabla c_s, \tag{A.17}$$

and

$$\vec{N} = -D_s \nabla c_s, \tag{A.18}$$

Eq. A.15 is transformed to the Eq. 26, that was used in the proposed modelling framework.

A.6. Comparison between 1D and 2D computational domain

The Fig. A.2 shows a computational domain of a full cell sandwich consisting of cathode, separator and anode component which is discretised either with 1D structured mesh across the cell or with 2D unstructured mesh. Computational meshes are generated with the open source mesher Gmsh and are imported to the proposed modelling framework, which supports both types of meshes, i.e. structured and unstructured types. Governing equations presented in Fig. 3 are solved implicitly in the computational domain for Li-ion concentration, solid- and liquid-phase potentials and temperature.

Consistently with Figs. 4 and A.3 presents results of the three analysed modelling approaches: Advanced Electrode Topology (AET), Newman primary particles and Newman secondary particles. Presented results clearly indicate that differences in results of discharge curves obtained with 1D and 2D computational domain differ negligibly for a particular modelling approach and that differences in modelling approaches to represent cathode material are much larger compared to the differences due to dimensionality of the computational domain. Similar trend can be observed for heat generation (Fig. A.4), where again differences in modelling approaches to represent cathode material are much larger compared to the differences due to dimensionality of the computational domain.
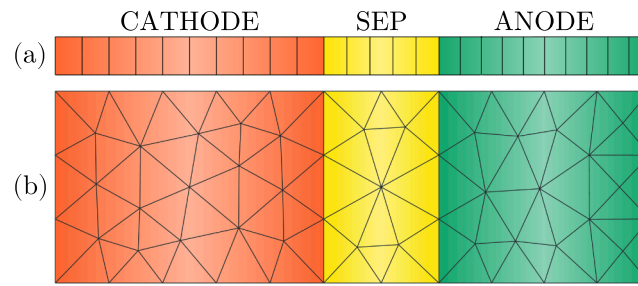
Fig. A.2. Representation of the computational domains with (a) 1D structured mesh containing 25 control volumes (10-5-10 for cathode-separator-anode) and (b) 2D unstructured mesh containing 100 control volumes (44-18-38 for cathode-separator-anode).
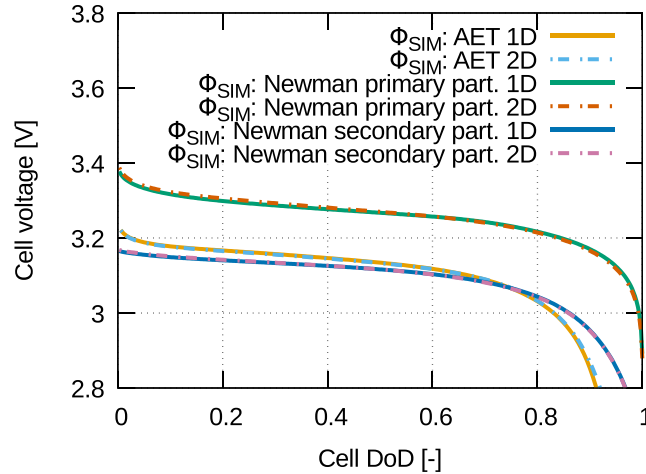

Fig. A.3. Comparison of the three simulated discharge characteristics at 2C modelled using a 1D computational domain from Fig. 4 (1D domain) with the corresponding results modelled using a 2D computational domain.
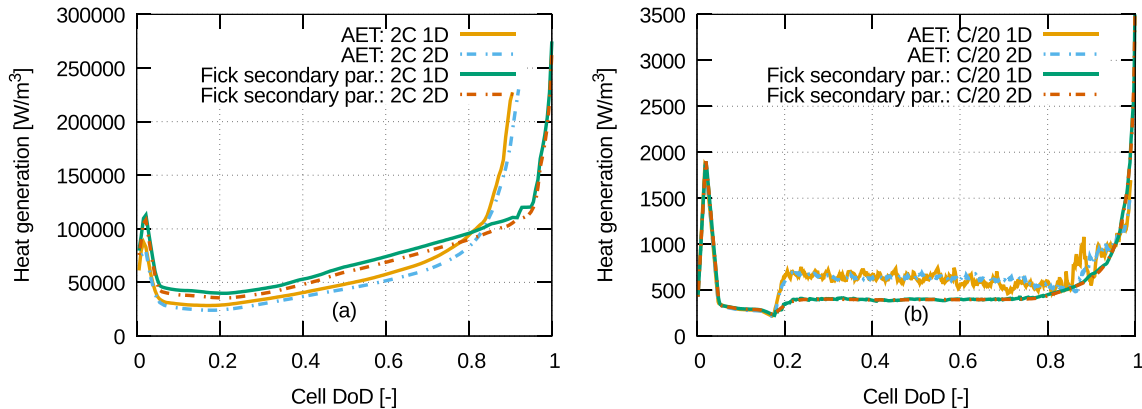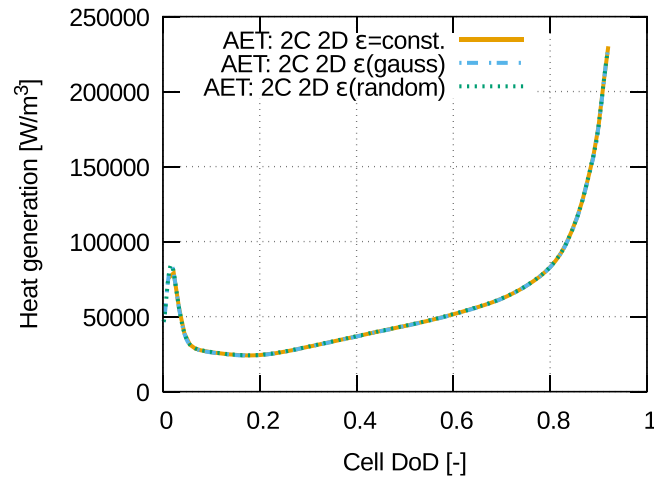

Fig. A.4. Comparison of the total heat generation in the cathode between AET and Newman secondary particles modelled using a 1D computational domain from Fig. 5 (1D domain) with the corresponding results modelled using a 2D computational domain for (a) higher 2C rate and (b) lower C/20 rate.

To further assess impact of spatial influences, Figs. A.5 and A.6 present impact of variation in porosity on the heat generation, which is a realistic case virtually representing nonuniformities in the production process. Fig. A.5 expectedly clearly shows interdependence between variation in porosity and local heat generation, which is an inherent results of coupled treatment of transport, electrochemical and heat generation phenomena. However, Fig. A.6 in addition shows that for the same average porosity and reasonable spatial porosity variation total heat generated in the cathode does not change notably. These results confirm that 1D model can be applied in a study aimed at modelling outbreak of the thermal runaway, as in such a study the heat up of the entire cell and thus total heat generation is most important, since temporally resolved temperature gradients are much
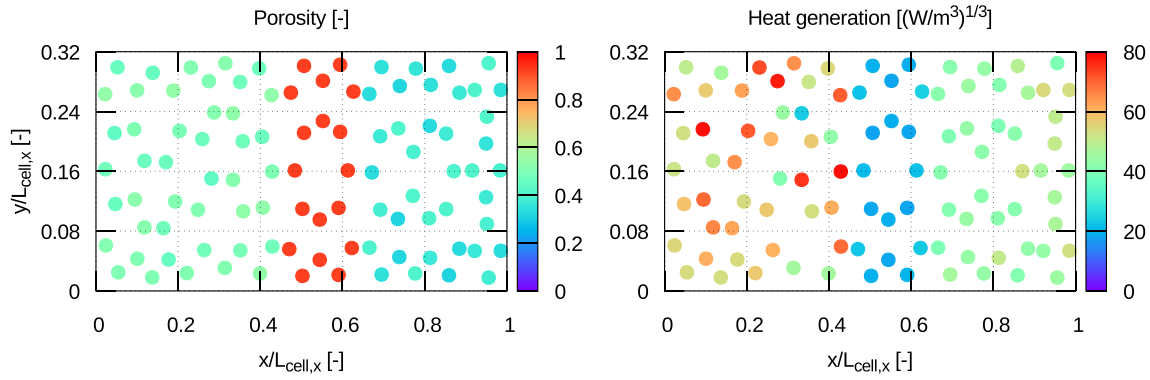
Fig. A.5. 2D representation of the randomly distributed porosity of 0.05 around $\overline{\epsilon}$ in both electrodes with constant values in the separator (left). Calculated spatially distributed heat generation with this variable porosity at the end of 2C discharge on the 2D computational domain (right). Total heat generation result from this case is shown in the Fig. A.6 under "AET: 2C 2D ϵ(random)" label in the legend.

Fig. A.6. Comparison of the total heat generation in the cathode with constant porosity $\overline{\epsilon}$, gaussian distributed porosity with standard deviation of 0.05 around $\overline{\epsilon}$ and randomly distributed porosity of 0.05 around $\overline{\epsilon}$ for AET model, 2D computational domain and with 2C rate.

larger compared to spatial intra-electrode temperature gradients.

This fact is also important in the view of computational times that increase with finer mesh, which is to a large extent related to increase in size of the Jacobian matrix. Compared to computational times of the model using 1D computational domain (Fig. A.2a), which are reported in Section 3.5, RT factor using 2D computational domain (Fig. A.2b) and and the time-step of 1 ms or frequency of 1 kHz equals around 667, whereas it reduces nearly linearly with the increased integration time step, as presented for the 1D model in Section 3.5.

Appendix B. Model parameters

This section presents model parameters used in the modelling framework. The parameters are divided into four groups. The parameters related to the electrolyte are listed in Table B.1. The parameters related to the electrode materials and separator are listed in Table B.2. Parameters related to the thermal model are listed in Table B.3. Finally, the parameters related to the anode degradation mechanisms are listed in Tables B.4 and B.5.

Table B.1
Model parameters for the electrolyte. References [61,39,62].

Parameter	Unit	Value
c_e^{ref}	mol/m^3	1000
D_e	m^2/s	$4 \cdot 10^{-10}$
T_{ref}	K	293.0
t_+	–	0.363

Table B.2

Model parameters for electrode materials and separator. Remarks: ‡full cell sandwich (assumed), *carbon coated LFP, ☆assumed. References [46,54,63,64].

Parameter	Unit	LFP	Graphite	Separator
brugg	–	1.5	1.5	1.5
c_p^{max}	mol/m^3	22,800	30,555	/
D_s	m^2/s	$5.0 \cdot 10^{-13}$	$3.9 \cdot 10^{-14}$	/
L	μm	70$^{‡☆}$	55$^{‡☆}$	30$^{‡☆}$
P	m/s	$5 \cdot 10^{-9☆}$	/	/
$\overline{R_p}$	m	$400 \cdot 10^{-9}$	$4.3 \cdot 10^{-6}$	/
T_{ref}	K	293.0	293.0	293.0
U^0	V	3.451	Table B.5	/
α	–	0.50	0.50	/
ϵ	–	0.49	0.36	0.92
$\varphi^{V,b+cf}$	–	0.05	0,05	/
σ	A/Vm	1.0*	68.58	/

Table B.3

Parameters of the thermal model. Thermal conductivity was assumed to be constant for a mixture (electrode, electrolyte, binder and carbon black) in the cross-plane direction of the electrode surface with value of 3.39 W/m^{2}K and in in-plane direction with value of 20.06 W/m^{2}K [65]. References [65–68].

Component	Density ρ [kg/m^3]	Specific heat c_p [J/kg K]
Electrolyte	1290.0	1580.0
LFP	1500.0	1260.0
Graphite	2660.0	709.0
Separator	492.0	1978.0
Binder + carbon black	1750.0	1120.0

Table B.4

Degradation model parameters. Remarks: ☆adjusted. References [18,28,69,9,70].

Parameter	Unit	Value
A_f^{Li-el}	1/s	$2.5 \cdot 10^{13}$
$A_f^{SEI_D}$	1/s	$1.66 \cdot 10^{15}$
$A_f^{e_D}$	1/s	$5.14 \cdot 10^{25}$
A_f^{pe}	1/s	$2.0 \cdot 10^{8}$
E_a^{Li-el}	J/mol	$1.32 \cdot 10^{5}$
$E_a^{SEI_D}$	J/mol	$1.38 \cdot 10^{5}$
$E_a^{e_D}$	J/mol	$2.7 \cdot 10^{5}$
E_a^{pe}	J/mol	$0.99 \cdot 10^{5}$
h_{Li-el}	J/mol	12352
h_{SEI_D}	J/mol	41634
h_{e_D}	J/mol	94181
h_{pe}	J/mol	30715
c_0^{EC}	mol/m^3	4541.0
D^{EC}	m^2/s	$2.0 \cdot 10^{-18}$
i_0^{LPL}	A/m^2	10^{-6}☆
k_0^{SEI}	m/s	$2.5 \cdot 10^{-16}$☆
M^{Li}	kg/mol	$6.49 \cdot 10^{-3}$
M^{SEI}	kg/mol	0.162
M^{LFP}	kg/mol	0.158
M^{e}	kg/mol	0.152
T_{ref}	K	293.0
U^{SEI}	V	0.4
α^{LPL}	–	0.5
α^{SEI}	–	0.5
κ^{SEI}	S/m	$1.75 \cdot 10^{-4}$
ρ^{Li}	kg/m^3	534
ρ^{SEI}	kg/m^3	1690.0
ω^{SEI}	–	1.0

Table B.5

Function dependencies for ionic conductivity κ_e, activity coefficient $\left(1 + \dfrac{\partial \ln f_\pm}{\partial \ln c_e}\right)$ and open circuit potential $U^0(x)$ for anode material. For the specific entropy $s_e(x)$, the values for both electrodes were extracted from plot in [63]. Note that the first two empiric equations take as an input electrolyte concentration c_e in units of mol/L.

Parameter	Unit	Function
$\kappa_e(c_e, T)$	A/Vm	$\dfrac{c_e}{10}(-10.5 + 0.074T - 6.96 \cdot 10^{-5}T^2 + 0.668c_e - 0.0178c_e T + 2.8 \cdot 10^{-5}c_e T^2 + 0.494c_e^2 - 8.86 \cdot 10^{-4}c_e T^2)^2$ [38,39]
$\left(1 + \dfrac{\partial \ln f_\pm}{\partial \ln c_e}\right)(c_e, T)$	–	$\dfrac{1}{1 - t_+}(0.601 - 0.24c_e^{0.25} + 0.982[1 - 0.0052(T - T_0)]c_e^{1.5})$ [38,39]
$U_{anode}^0(x)$	V	$0.7222 + 0.1387x + 0.029x^{0.5} - 0.0172x^{-1} + 0.0019x^{-1.5} + 0.2808\exp(0.90 - 15x) - 0.7984\exp(0.4465x - 0.4108)$ [64]
$s_e(x)$	J/mol K	Numeric table extracted from [63].

References

[1] Battery2030 initiative. URL:https://battery2030.eu/research/roadmap/. [Accessed: 2020-11-15].

[2] Liu C, Neale ZG, Cao G. Understanding electrochemical potentials of cathode materials in rechargeable batteries. Mater Today 2016;19(2):109–23. https://doi.org/10.1016/j.mattod.2015.10.009.

[3] Mele U, Pačnik I, Zelič K, Moškon J, Katrašnik T. Advanced porous electrode modelling framework based on more consistent virtual representation of the electrode topology. J Electrochem Soc 167 (6). doi:10.1149/1945-7111/ab84fb.

[4] Wang J, Kim H, Hyun H, Jo S, Han J, Ko D, Seo S, Kim J, Kong H, Lim J. Probing and resolving the heterogeneous degradation of nickel-rich layered oxide cathodes across multi-length scales. Small Methods 2020;4(10):2000551. https://doi.org/10.1002/smtd.202000551.

[5] Schlasza C, Ostertag P, Chrenko D, Kriesten R, Bouquain D. Review on the aging mechanisms in Li-ion batteries for electric vehicles based on the FMEA method. In: 2014 IEEE transportation electrification conference and expo (ITEC); IEEE, 2014. p. 1–6.

[6] Feng X, Ouyang M, Liu X, Lu L, Xia Y, He X. Thermal runaway mechanism of lithium ion battery for electric vehicles: a review (2018). doi:10.1016/j. ensm.2017.05.013.

[7] MacNeil DD, Christensen L, Landucci J, Paulsen JM, Dahn JR. An autocatalytic mechanism for the reaction of LixCoO2 in electrolyte at elevated temperature. J Electrochem Soc 2000;147(3):970. https://doi.org/10.1149/1.1393299.

[8] Liu X, Ren D, Hsu H, He X, Liu X, Ren D, Hsu H, Feng X, Xu G-L, Zhuang M. Thermal runaway of lithium-ion batteries without internal short circuit thermal runaway of lithium-ion batteries without internal short circuit. Joule 2018:1–18. https://doi.org/10.1016/j.joule.2018.06.015. URL:https://doi.org/10.1016/j. joule.2018.06.015.

[9] Abada S, Petit M, Lecocq A, Marlair G, Sauvant-Moynot V, Huet F. Combined experimental and modeling approaches of the thermal runaway of fresh and aged lithium-ion batteries. J Power Sources 2018;399:264–73. https://doi.org/10.1016/ j.jpowsour.2018.07.094.

[10] Li D, Danilov DL, Zwikirsch B, Fichtner M, Yang Y, Eichel RA, Notten PH. Modeling the degradation mechanisms of C6/LiFePO4 batteries. J Power Sources 2018;375: 106–17. https://doi.org/10.1016/j.jpowsour.2017.11.049.

[11] Horstmann B, Single F, Latz A. Review on multi-scale models of solid-electrolyte interphase formation (feb 2019). doi:10.1016/j.coelec.2018.10.013.

[12] Huang W, Attia PM, Wang H, Renfrew SE, Jin N, Das S, Zhang Z, Boyle DT, Li Y, Bazant MZ, McCloskey BD, Chueh WC, Cui Y. Evolution of the solid-electrolyte interphase on carbonaceous anodes visualized by atomic-resolution cryogenic electron microscopy. Nano Lett 2019;19:5140–8. https://doi.org/10.1021/acs. nanolett.9b01515. URL:http://pubs.acs.org/doi/10.1021/acs.nanolett.9b01515.

[13] von Kolzenberg L, Latz A, Horstmann B. Solid-electrolyte interphase during battery cycling: theory of growth regimes. ChemSusChem 13 (15): 2020; 3901–3910. arXiv:2004.01458, doi:10.1002/cssc.202000867.

[14] Kim SP, Duin AC, Shenoy VB. Effect of electrolytes on the structure and evolution of the solid electrolyte interphase (SEI) in Li-ion batteries: a molecular dynamics study. J Power Sources 2011;196(20):8590–7. https://doi.org/10.1016/j. jpowsour.2011.05.061.

[15] Single F, Horstmann B, Latz A. Revealing SEI morphology: in-depth analysis of a modeling approach. J Electrochem Soc 2017;164(11):E3132–45. https://doi.org/ 10.1149/2.0121711jes.

[16] Li D, Danilov DL, Xie J, Raijmakers L, Gao L, Yang Y, Notten PH. Degradation mechanisms of C6/LiFePO4 batteries: experimental analyses of calendar aging. Electrochim Acta 2016;190:1124–33. https://doi.org/10.1016/j. electacta.2015.12.161.

[17] Gu Y, Wang W-W, Li Y-J, Wu Q-H, Tang S, Yan J-W, Zheng M-S, Wu D-Y, Fan C-H, Hu W-Q, Others. Designable ultra-smooth ultra-thin solid-electrolyte interphases of three alkali metal anodes. Nat Commun 9 (1): 2018; 1–9.

[18] Feng X, He X, Ouyang M, Wang L, Lu L, Ren D, Santhanagopalan S. A coupled electrochemical-thermal failure model for predicting the thermal runaway behavior of lithium-ion batteries. J Electrochem Soc 2018;165(16):A3748–65. https://doi.org/10.1149/2.0311816jes.

[19] Kriston A, Adanouj I, Ruiz V, Pfrang A. Quantification and simulation of thermal decomposition reactions of Li-ion battery materials by simultaneous thermal analysis coupled with gas analysis. J Power Sources 435. doi:10.1016/j. jpowsour.2019.226774.

[20] Franco AA. Multiscale modelling and numerical simulation of rechargeable lithium ion batteries: concepts, methods and challenges. RSC Adv 2013;3(32):13027–58. https://doi.org/10.1039/c3ra23502e.

[21] Franco AA, Rucci A, Brandell D, Frayret C, Gaberšček M, Jankowski P, Johansson P. Boosting rechargeable batteries R&D by multiscale modeling: myth or reality? Chem Rev 2019;119:4569–627. https://doi.org/10.1021/acs. chemrev.8b00239. URL:http://pubs.acs.org/doi/10.1021/acs.chemrev.8b00239 https://pubs.acs.org/doi/10.1021/acs.chemrev.8b00239.

[22] Newman J, Tiedemann W. Porous-electrode theory with battery applications. AIChE J 1975;21(1):25–41. https://doi.org/10.1002/aic.690210103. URL:http:// doi.wiley.com/10.1002/aic.690210103l.

[23] Mao Z, Farkhondeh M, Pritzker M, Fowler M, Chen Z. Multi-particle model for a commercial blended lithium-ion electrode. J Electrochem Soc 2016;163(3): A458–69. https://doi.org/10.1149/2.0321603jes. URL:http://jes.ecsdl.org/ content/163/3/A458.abstract.

[24] An Z, Jia L, Wei L, Dang C, Peng Q. Investigation on lithium-ion battery electrochemical and thermal characteristic based on electrochemical-thermal coupled model. Appl Therm Eng 2018;137:792–807. https://doi.org/10.1016/j. applthermaleng.2018.04.014.

[25] Li J, Cheng Y, Jia M, Tang Y, Lin Y, Zhang Z, Liu Y. An electrochemical-thermal model based on dynamic responses for lithium iron phosphate battery. J Power Sources 2014;255:130–43. https://doi.org/10.1016/j.jpowsour.2014.01.007.

[26] Dreyer W, Jamnik J, Guhlke C, Huth R, Moškon J, Gaberšček M. The thermodynamic origin of hysteresis in insertion batteries. Nat Mater 2010;9(5): 448–53. https://doi.org/10.1038/nmat2730. URL:http://www.ncbi.nlm.nih.gov/ pubmed/20383130.

[27] Islam MM, Van Duin AC. Reductive decomposition reactions of ethylene carbonate by explicit electron transfer from lithium: an eReaxFF molecular dynamics study. J Phys Chem C 2016;120(48):27128–34. https://doi.org/10.1021/acs. jpcc.6b08688.

[28] Yang XG, Leng Y, Zhang G, Ge S, Wang CY. Modeling of lithium plating induced aging of lithium-ion batteries: transition from linear to nonlinear aging. J Power Sources 2017;360:28–40. https://doi.org/10.1016/j.jpowsour.2017.05.110.

[29] Zelič K, Katrašnik T. Thermodynamically consistent derivation of chemical potential of a battery solid particle from the regular solution theory applied to LiFePO4. Sci Rep 9 (1). doi:10.1038/s41598-019-38635-2.

[30] Zelič K, Katrašnik T. Thermodynamically consistent and computationally efficient 0D lithium intercalation model of a phase separating cathode particle. J Electrochem Soc 2019;166(14):A3242–9. https://doi.org/10.1149/ 2.0381914jes. URL:http://jes.ecsdl.org/lookup/doi/10.1149/2.0381914jes.

[31] Orvananos B, Malik R, Yu HC, Abdellahi A, Grey CP, Ceder G, Thornton K. Architecture dependence on the dynamics of nano-LiFePO4 electrodes. Electrochim Acta 2014;137:245–57. https://doi.org/10.1016/j. electacta.2014.06.029. URL:https://doi.org/10.1016/j.electacta.2014.06.029.

[32] Shurtz RC, Engerer JD, Hewson JC. Predicting high-temperature decomposition of lithiated graphite: Part I. Review of phenomena and a comprehensive model. J Electrochem Soc 2018;165(16):A3878–90. https://doi.org/10.1149/ 2.0541816jes.

[33] Saw LH, Ye Y, Tay AA. Electrochemical-thermal analysis of 18650 Lithium Iron Phosphate cell. Energy Convers Manage 2013;75:162–74. https://doi.org/ 10.1016/j.enconman.2013.05.040.

[34] Rao M, Zhang L, Li L, Rong L, Ye C, Zhou G, Xu H, Qiu Y. Investigation of lithium content changes to understand the capacity fading mechanism in LiFePO4/graphite battery. J Electroanal Chem 853. doi:10.1016/j.jelechem.2019.113544.

[35] Waldmann T, Wilka M, Kasper M, Fleischhammer M, Wohlfahrt-Mehrens M. Temperature dependent ageing mechanisms in Lithium-ion batteries – a Post-Mortem study. J Power Sources 2014;262:129–35. https://doi.org/10.1016/j. jpowsour.2014.03.112.

[36] Richard MN, Dahn JR. Accelerating rate calorimetry study on the thermal stability of lithium intercalated graphite in electrolyte. II. Modeling. J Electrochem Soc 1999;146(6):2068–77. https://doi.org/10.1149/1.1391893.

[37] Ashwin TR, Chung YM, Wang J. Capacity fade modelling of lithium-ion battery under cyclic loading conditions. J Power Sources 2016;328:586–98. https://doi. org/10.1016/j.jpowsour.2016.08.054.

[38] Kosch S, Zhao Y, Sturm J, Schuster J, Mulder G, Ayerbe E, Jossen A. A computationally efficient multi-scale model for Lithium-Ion cells. J Electrochem Soc 2018;165(10):A2374–88. https://doi.org/10.1149/2.1241810jes.

[39] Valoen LO, Reimers JN. Transport properties of LiPF6-based Li-Ion battery electrolytes. J Electrochem Soc 2005;152(5):A882. https://doi.org/10.1149/ 1.1872737.

[40] Latz A, Zausch J. Thermodynamic consistent transport theory of Li ion batteries. Bericht 195 (195).

[41] Hosseinzadeh E, Genieser R, Worwood D, Barai A, Marco J, Jennings P. A systematic approach for electrochemical-thermal modelling of a large format lithium-ion battery for electric vehicle application. J Power Sources 2018;382: 77–94. https://doi.org/10.1016/j.jpowsour.2018.02.027.

[42] Bai P, Cogswell DA, Bazant MZ. Suppression of phase separation in LiFePO4 nanoparticles during battery discharge. Nano Lett 11 (11): 2011; 4890–4896. arXiv:1108.2326, doi:10.1021/nl202764f.

[43] Lim J, Li Y, Alsem DH, So H, Lee SC, Bai P, Cogswell DA, Liu X, Jin N, Yu Y-S, Salmon NJ, Shapiro DA, Bazant MZ, Tyliszczak T, Chueh WC. Origin and hysteresis of lithium compositional spatiodynamics within battery primary particles. Science 2016;27(2004):566–71.

[44] Pinson MB, Bazant MZ. Theory of SEI formation in rechargeable batteries: capacity fade, accelerated aging and lifetime prediction. J Electrochem Soc 160 (2): 2012; A243–A250. arXiv:1210.3672, doi:10.1149/2.044302jes. URL:http://jes.ecsdl. org/cgi/doi/10.1149/2.044302jes.

[45] Hatchard TD, MacNeil DD, Basu A, Dahn JR. Thermal model of cylindrical and prismatic Lithium-Ion cells. J Electrochem Soc 2001;148(7):A755. https://doi.org/ 10.1149/1.1377592.

[46] Fink C, Kaltenegger B. Electrothermal and electrochemical modeling of Lithium-ion batteries: 3D simulation with experimental validation. ECS Trans 2014;61(27): 105–24. https://doi.org/10.1149/06127.0105ecst.

[47] Shurtz RC, Engerer JD, Hewson JC. Predicting high-temperature decomposition of lithiated graphite: Part II. Passivation layer evolution and the role of surface area. J Electrochem Soc 2018;165(16):A3891–902. https://doi.org/10.1149/ 2.0171814jes.

[48] Shurtz RC, Engerer JD, Hewson JC. Predicting high-temperature decomposition of lithiated graphite: Part I. Review of phenomena and a comprehensive model. J Electrochem Soc 2018;165(16):A3878–90. https://doi.org/10.1149/ 2.0541816jes.

[49] Li Y, El Gabaly F, Ferguson TR, Smith RB, Bartelt NC, Sugar JD, Fenton KR, Cogswell DA, Kilcoyne ALD, Tyliszczak T, Bazant MZ, Chueh WC. Current-induced transition from particle-by-particle to concurrent intercalation in phase-separating battery electrodes. Nat Mater 13 (12): 2014; 1149–1156. doi:10.1038/nmat4084.

[50] Press WH, Teukolsky SA, Vetterling WT, Flannery BP. Numerical recipes 3rd edition: the art of scientific computing. Cambridge University Press; 2007.

[51] Battery interface genome - materials acceleration platform (big-map), URL:https:// www.big-map.eu, accessed: 2021-01-31.

[52] Doyle M, Fuller TF, Newman J. Modeling of galvanostatic charge and discharge of the lithium/polymer/insertion cell. J Electrochem Soc 140: 1993; 1526–1533.

[53] Bruggeman DAG. Berechnung verschiedener physikalischer Konstanten von heterogenen Substanzen. I. Dielektrizitätskonstanten und Leitfähigkeiten der Mischkörper aus isotropen Substanzen. Ann Phys 1935;416(8):665–79. https:// doi.org/10.1002/andp.19354160802.

[54] Doyle M, Newman J, Gozdz AS, Schmutz CN, Tarascon J-M. Comparison of modeling predictions with experimental data from plastic lithium ion cells. J Electrochem Soc 1996;143(6):1890–903.

[55] Colclasure AM, Kee RJ. Thermodynamically consistent modeling of elementary electrochemistry in lithium-ion batteries. Electrochim Acta 2010;55(28):8960–73. https://doi.org/10.1016/j.electacta.2010.08.018. URL:https://doi.org/10.1016/j. electacta.2010.08.018.

[56] Ferguson TR, Bazant MZ. Phase transformation dynamics in porous battery electrodes. Electrochim Acta 2014;146:89–97. https://doi.org/10.1016/j.electacta.2014.08.083. arXiv:1401.7072 URL:https://doi.org/10.1016/j.electacta.2014.08.083.

[57] Zhang P, Wu Y, Zhang D, Xu Q, Liu J, Ren X, Luo Z, Wang M, Hong W. Molecular dynamics study on ion diffusion in LiFePO4 olivine materials. J Phys Chem A 2008;112(24):5406–10. https://doi.org/10.1021/jp710204z.

[58] Smith RB, Khoo E, Bazant MZ. Intercalation kinetics in multiphase-layered materials. J Phys Chem C 121 (23): 2017; 12505–12523. arXiv:1701.08858, doi:10.1021/acs.jpcc.7b00185.

[59] Guo Y, Smith RB, Yu Z, Efetov DK, Wang J, Kim P, Bazant MZ, Brus LE. Li intercalation into graphite: direct optical imaging and Cahn-Hilliard reaction dynamics. J Phys Chem Lett 2016;7(11):2151–6. https://doi.org/10.1021/acs.jpclett.6b00625.

[60] Orvananos B, Ferguson TR, Yu H-C, Bazant MZ, Thornton K. Particle-level modeling of the charge-discharge behavior of nanoparticulate phase-separating Li-Ion battery electrodes. J Electrochem Soc 2014;161(4):A535–46. https://doi.org/10.1149/2.024404jes. arXiv:arXiv:1309.6495v1 URL:http://jes.ecsdl.org/content/161/4/A535%5Cnhttp://jes.ecsdl.org/content/161/4/A535.full.pdf.

[61] Wu B, Yufit V, Marinescu M, Offer GJ, Martinez-Botas RF, Brandon NP. Coupled thermal-electrochemical modelling of uneven heat generation in lithium-ion battery packs. J Power Sources 2013;243:544–54. https://doi.org/10.1016/j.jpowsour.2013.05.164.

[62] Nishida T, Nishikawa K, Fukunaka Y. Diffusivity measurement of LiPF6, LiTFSI, LiBF4 in PC. ECS Trans 2008;6(18):1–14. https://doi.org/10.1149/1.2831921.

[63] Xu M, Zhang Z, Wang X, Jia L, Yang L. A pseudo three-dimensional electrochemical-thermal model of a prismatic LiFePO4 battery during discharge process. Energy 2015;80:303–17. https://doi.org/10.1016/j.energy.2014.11.073.

[64] Boovaragavan V, Harinipriya S, Subramanian VR. Towards real-time (milliseconds) parameter estimation of lithium-ion batteries using reformulated physics-based models. J Power Sources 2008;183(1):361–5. https://doi.org/10.1016/j.jpowsour.2008.04.077.

[65] Maleki H, Al Hallaj S, Selman JR, Dinwiddie RB, Wang H. Thermal properties of lithium-ion battery and components. J Electrochem Soc 1999;146(3):947–54. https://doi.org/10.1149/1.1391704.

[66] Lopez CF, Jeevarajan JA, Mukherjee PP. Characterization of lithium-ion battery thermal abuse behavior using experimental and computational analysis. J Electrochem Soc 2015;162(10):A2163–73. https://doi.org/10.1149/2.0751510jes. URL:http://jes.ecsdl.org/lookup/doi/10.1149/2.0751510jes.

[67] Benger R, Wenzl H, Beck H-P, Jiang M, Ohms D, Schaedlich G. Electrochemical and thermal modeling of lithium-ion cells for use in HEV or EV application. World Electric Vehicle J 2009;3(2):342–51.

[68] Eshetu GG, Grugeon S, Laruelle S, Boyanov S, Lecocq A, Bertrand JP, Marlair G. In-depth safety-focused analysis of solvents used in electrolytes for large scale lithium ion batteries. Phys Chem Chem Phys 2013;15(23):9145–55. https://doi.org/10.1039/c3cp51315g.

[69] Lee CH, Bae SJ, Jang M. A study on effect of lithium ion battery design variables upon features of thermal-runaway using mathematical model and simulation. J Power Sources 2015;293:498–510. https://doi.org/10.1016/j.jpowsour.2015.05.095.

[70] Prada E, Di Domenico D, Creff Y, Bernard J, Sauvant-Moynot V, Huet F. A simplified electrochemical and thermal aging model of LiFePO4-graphite Li-ion batteries: power and capacity fade simulations. J Electrochem Soc 2013;160(4):A616–28. https://doi.org/10.1149/2.053304jes.